CFD Simulation of a Pre-Chamber Spark-ignition Large Bore CNG Engine: Model Development, Practical Applications, and Experimental Validation

Soo-Jin Jeong *, Seokpan Seo , Seong-Joon Moon

Posted Date: 4 March 2025

doi: 10.20944/preprints202503.0200.v1

Keywords: Natural Gas; Active Pre-chamber; Computational Fluid Dynamics; Pre-Chamber Spark Ignition (PCSI); Lean-premixed natural gas combustion; Turbulent Jet Ignition; Flame Speed; Exhaust Emission

 doi:10.20944/preprints202503.0200.v1

Article

CFD Simulation of a Pre-Chamber Spark-Ignition Large Bore CNG Engine: Model Development, Practical Applications, and Experimental Validation

Soo-Jin Jeong [1,*], Seokpan Seo [2] and Seong-Joon Moon [1]

[\1] Korea Automotive Technology Institute, 303 Pungse-myeon, Dongnam-gu, Cheonan-si 31214, Republic of Korea

[2] STX Engine Co., Ltd., 36, Gongdan-ro, 474 beon-gil, Seongsan-gu, Changwon-si, Gyeongsangnam-do, 51574, Republic of Korea

* Correspondence: sjjeong@katech.re.kr; Tel.: +82-41-559-3059

Abstract: This study develops and validates a three-dimensional CFD model for a 12-liter large-bore active-type pre-chamber spark-ignition (PCSI) engine fueled by natural gas. The model incorporates an advanced Extended Coherent Flamelet Model (ECFM-3Z) with a tuned stretch factor to capture complex turbulence–flame interactions, flame propagation, and pollutant formation under ultra-lean conditions. By systematically varying pre-chamber geometries—specifically orifice diameter, cone angle, diverging-tapered nozzle and volume—the simulations assess their effects on combustion dynamics, heat release rates, turbulent jet penetration, and emissions (NOx and CO). Model predictions of in-cylinder and pre-chamber pressure profiles, combustion phasing, and emission trends are validated against experimental data. The results demonstrate that optimizing pre-chamber and orifice configurations enhances turbulent mixing, accelerates flame development, and reduces local high-temperature zones, thereby suppressing NOx and CO formation. Although some discrepancies in NOx predictions persist due to limitations in current turbulence–chemistry models, the findings offer valuable insights for the design of high-efficiency, low-emission PCSI engines.

Keywords: natural gas; active pre-chamber; computational fluid dynamics; pre-chamber spark ignition (PCSI); lean-premixed natural gas combustion; turbulent jet ignition; flame speed; exhaust emission

1. Introduction

The global focus on clean and efficient combustion has positioned pre-chamber spark-ignition (PCSI) engines as a key technology for high thermal efficiency and low emissions, especially with compressed natural gas (CNG) [1–6]. PCSI engines enhance combustion stability, fuel-air mixing, and temperature uniformity, reducing NOx emissions compared to conventional spark-ignition systems [7–9]. However, optimizing turbulence, chemical kinetics, and combustion interactions remains challenging, necessitating advanced numerical simulations [9–11].

PCSI engines face combustion stability and emission control challenges, particularly in large-bore applications where conventional ignition struggles with complete combustion [1–4,10]. Computational Fluid Dynamics (CFD) provides detailed combustion insights, reducing reliance on experimental methods. Kirkpatrick et al. [1] demonstrated CFD's capability in modeling fuel injection, combustion, and flame propagation, while pre-chamber technology mitigates CNG's lower flame speeds and turbulence issues in Miller cycle engines [2,10].

CFD modeling for gas-fueled pre-chamber engines has evolved from 2D to advanced 3D simulations, improving predictive accuracy. Studies [11–13] validated CFD models' reliability in combustion analysis, and Winter et al. [4] highlighted CFD's role in mixing optimization and combustion enhancement. These advancements enable precise ignition delay predictions, air-fuel

 doi:10.20944/preprints202503.0200.v1

mixture optimization, and pollutant formation assessment in gas-fueled engines. Recent advancements in CFD modeling have shifted toward highly sophisticated three-dimensional approaches incorporating detailed chemical reaction mechanisms and advanced turbulence-flame interaction related models. A detailed account of the CFD model and an extensive review of the various modeling techniques reported in the literature are provided in references [10,14]. Methods such as Large Eddy Simulation (LES) and Direct Numerical Simulation (DNS) provide deeper insights into critical phenomena, including jet ignition dynamics, flame quenching, stratified mixture formation, and pollutant generation [14–17]. Additionally, studies on methane-fueled turbulent jet ignition systems emphasize the significance of adaptive mesh refinement (AMR) techniques in accurately resolving pre-chamber orifice flow structures and combustion processes [2,3,5,12,14]. As a result, detailed CFD analyses have enabled the aforementioned studies to clarify the interaction between combustion and turbulence in PCSI engines, thereby enhancing our understanding of the system's characteristics and inherent limitations. Until now, CFD analysis techniques have been utilized in the design of PCSI engines to optimize pre-chamber volume, orifice diameter, injected fuel mass, and spark timing for lean combustion [5,6,13–15,18–23]. These studies have also aimed to elucidate the trade-offs between pre-chamber volume and nozzle area in terms of scavenging efficiency, combustion efficiency and emissions. This involves complex interactions influencing turbulence generation, fuel-air mixing, flame propagation, and pollutant formation. Recently, several noteworthy studies related to CFD have emerged, including the following: Bigalli et al. [5] conducted comprehensive numerical investigations of various passive pre-chamber geometries using detailed chemistry solvers, demonstrating that optimizing pre-chamber design significantly improves combustion efficiency and reduces emissions. Advanced modeling techniques have also facilitated the detailed analysis of spark timing effects. For instance, Xue et al. [6] showed how variations in spark timing influence turbulent jet characteristics and overall engine performance in lean-burn natural gas engines. These developments have enhanced simulations of hydrogen and CNG fuels, though challenges such as high computational costs and model validation persist. Xu et al. [15] also focused on the effects of spark timing and pre-chamber global equivalence ratio on turbulent jet ignition behavior, using detailed CFD model with a reduced methane mechanism and LES turbulence model.

Despite these advancements, significant challenges remain in developing comprehensive, experimentally validated CFD models tailored for large-bore CNG PCSI engines because the ignition mechanism in the main chamber induced by the turbulent hot jets arising from the nozzles is profoundly different from a conventional turbulent premixed flame development [14,15,17]. One of the most significant characteristics of PCSI engines is their multi-mode combustion behavior. Previous studies[10,14,24–26] have well documented that in PCSI engines, turbulent lean-premixed flames exhibit an expanded reaction zone as the Reynolds number increases and the Karlovitz number exceeds unity (Ka > 1), with certain regions showing particularly extensive reaction zones. In PCSI engines, the primary combustion regimes are the flamelet and Thin Reaction Zones (TRZ) regimes, both of which correspond to turbulent flames characterized by moderate to high Karlovitz numbers. However, nearly all studies to date that have examined the combustion characteristics of PCSI engines using CFD techniques have relied on combustion models based on the assumptions of the flamelet regime—where the quasi-steady laminar flame structure, typically observed in the corrugated flamelet regime, is disrupted. As a result, these models struggle to accurately capture the combustion behavior in medium and high Karlovitz number regimes. Therefore, in the absence of a numerical model capable of accurately representing the physics of turbulent jet ignition combustion, several recent studies have attempted an alternative approach. These efforts involve the ad hoc tuning of model constants associated with large- and small-scale turbulence enhancements, as well as the flame stretch factor, by comparing them with experimental data. Through this approach, existing flamelet-based combustion models have been adapted and improved for application in the combustion analysis of PCSI engines [10,14,26,27]. However, these approaches may not sufficiently align numerical simulations with experimental data in both the pre-chamber and main combustion

 doi:10.20944/preprints202503.0200.v1

chamber [10,14,26]. To address the limitations of RANS-based turbulence and flamelet-based combustion models in capturing turbulence–flame interactions, studies have focused on refining model coefficients governing combustion speed and burn rate.

Notwithstanding these developments in CFD methodologies, a key limitation of numerical models is their accuracy in predicting emissions in PCSI engines. This is critical, as PCSI technology in large-bore natural gas engines aims to extend the lean-burn limit while reducing NOx emissions. Extensive CFD-based investigations have analyzed the effects of pre-chamber design parameters—such as number of orifice, diameter, inclination angle, and volume—on NOx formation[19,20,28]. Additionally, CFD models have provided insights into pre-chamber combustion physics and chemistry, which are difficult to capture experimentally [12,29]. However, experimental validation of NOx predictions and in-pre and main chamber chemical kinetics remains insufficient, highlighting the need for further empirical studies. Existing CFD frameworks often oversimplify the effects of residual gas interactions and omit secondary NOx formation pathways, such as prompt NO and the NNH mechanism. Moreover, these models typically require extensive geometry-specific calibration, limiting their generalizability. Variability in NOx prediction accuracy frequently arises from simplified representations of phenomena such as turbulent flame interactions, residual gas effects, transient combustion dynamics, and ultra-lean operational conditions.

Recent advancements in numerical modeling have sought to address these challenges by integrating Computational Fluid Dynamics (CFD) with machine learning (ML) techniques [30,31]. Posch et al. [30] introduced an ML-based approach for pre-chamber design optimization, condensing 3D CFD simulations into simplified models for predicting pressure differentials and NOx levels. While achieving <10% deviation, this method relied on trend analysis rather than absolute performance predictions due to condensed simulation data limitations. To address these challenges, further refinement of high-fidelity CFD-ML hybrid models is essential to enhance scalability and accuracy. Future research should focus on improving transient condition predictions, enabling models to capture real-world variations in load and speed. This advancement is crucial for optimizing PCSI engine performance while reducing computational costs and ensuring robust emission predictions.

Even with these notable improvements, several limitations persist in existing models, including insufficient experimental validation for large-bore engines and limited studies on multi-fuel applications. Until now, CFD studies on PCSI engines utilizing natural gas as a fuel have been limited to engines with displacements ranging from 0.5 liters to 6 liters [18,19,21,22,32,33]. Only recently has a CFD-based numerical study been conducted to examine the effects of nozzle diameter, hole number, and hole orientation on the combustion and scavenging characteristics of a 12-liter passive-type PCSI large-bore CNG engine [20]. As widely recognized, the implementation of the pre-chamber spark ignition (PCSI) combustion method in large-displacement engines poses considerable challenges due to increased combustion chamber volume, prolonged flame propagation distances, and greater heat transfer losses, all of which impact combustion efficiency and stability. Ensuring uniform fuel distribution and stable ignition timing becomes more difficult, leading to combustion instability and efficiency losses. Additionally, reduced charge motion and inadequate jet penetration hinder complete combustion, while higher in-cylinder pressures increase knock tendencies. Scaling PCSI technology requires optimized pre-chamber design, injector placement, and ignition control. Addressing these challenges necessitates advanced CFD simulations and refined combustion strategies to enhance performance and efficiency in large-displacement engines.

As described earlier, several limitations persist in existing CFD models for PCSI engines, particularly in active type large-bore PCSI applications, including insufficient experimental validation and limited studies on emissions and chemical kinetics. Therefore, this study aims to address these limitations by developing and validating a detailed three-dimensional CFD model specifically for 12-liter large-bore active-type pre-chamber spark-ignition engines fueled by natural gas, a topic that has not been extensively studied. Particular emphasis is placed on practical applications and experimental validation to enhance model reliability. The work also integrates

 doi:10.20944/preprints202503.0200.v1

insights from various studies, including those by previous literatures [10,14,17,25–27], to enhance understanding of ignition mechanisms and improve overall engine performance while reducing emissions. In this study, experimental data and a 0D/1D system-level simulation program were utilized to establish accurate initial and boundary conditions. To ensure precise combustion modeling, a well-tuned version of the ECFM-3Z model, refined through experimental calibration of the stretch factor in a flamelet-based combustion model, was employed. Using this approach, the effects of pre-chamber orifice geometry and cone angle variations on the chemical processes and combustion characteristics within both the pre-chamber and main chamber of the target engine were analyzed. Additionally, the impact of these design variations on pollutant formation, specifically CO and NOx emissions, was examined in detail.

2. Experimental Set up and Test Engine

2.1. Test Cell and Engine Specification

The pre-chamber combustion system investigated in this study was implemented in a turbocharged eight-cylinder port fuel injection (PFI) spark-ignition (SI) engine, incorporating turbulent jet ignition (TJI) technology from Korea STX Engine Company. Figure 1 provides a schematic representation of the engine configuration. To ensure homogeneous air-fuel mixing, the PFI system was positioned 353 mm upstream of the cylinder head within the intake manifold. The cylinder head featured four valves per cylinder with double overhead camshafts (DOHC) to enhance cylinder filling and scavenging efficiency. A Miller cycle strategy with late intake valve closing was applied to reduce NOx emissions and improve thermal efficiency. The engine was coupled to a 3,600 kW hydraulic dynamometer, controlled via a Horiba SPARCE dynamometer system, under steady-state operating conditions. In-cylinder pressure was measured using a Dewetron combustion analyzer (DEWE-800-CA2) equipped with a high-temperature pressure sensor. Under steady-state operation, a National Instruments LabVIEW control system governing the engine actuators and sensors enables the combustion analyzer to record 300 cycles of pressure data at a 0.1 CAD sampling rate, capturing detailed pressure traces and other averaged cycle measurements at a lower resolution. Fuel and coolant temperatures were maintained constant through testbed cooling facilities, while fuel mass flow was recorded using an orifice-type flowmeter.

Exhaust gas emissions, including NO, total hydrocarbons (THC), and CO, O_2, CO_2 were analyzed using a HORIBA MEXA-ONE exhaust gas analyzer at the exhaust port outlet. Additionally, particulate matter (PM) emissions were quantified using an AVL PM Sampler smoke meter.

The target engine was an eight-cylinder, pre-mixed spark-ignition engine fueled with natural gas. Experimental tests were conducted under steady-state conditions across load variations ranging from 10% to 100%, with results serving as benchmark data for CFD simulation validation. Detailed engine specifications and operating conditions are presented in Tables 1 and 2.

Table 1. Engine specifications.

Engine	4 Stroke SI
Number of cylinders	8
Displacement / 1 cylinder	11.4 liter
Bore[mm]	220
Stroke[mm]	300
Compression Ratio	14:1
Connecting Rod Length	630mm
Swirl Ratio	0.024(averaged)
Intake valve open and closing strategy	Miller cycle
Rated Engine speed[rpm]	1000

Table 2. Operating conditions.

 doi:10.20944/preprints202503.0200.v1

Engine	Specification
Speed [rpm]	1000
Load	Full load
Intake port pressure[bar]	4.271
Intake port temperature [℃]	37.74
Intake mass flow rate [kg/h]	8,477
λ (Main chamber)	2
Exhaust manifold pressure [℃]	3.87
Exhaust port temperature [℃]	489.6
Spark timing [CA BTDC]	13.41
Start of Injection timing (@ main) [CA BTDC]	330.11
Fuel injection duration (@ main) [CA]	48.66
Start of Injection timing (@ pre-chamber) [CA BTDC]	231.2
Fuel injection duration (@pre-chamber) [CA]	101.4
Fuel injection temperature [℃]	15.07

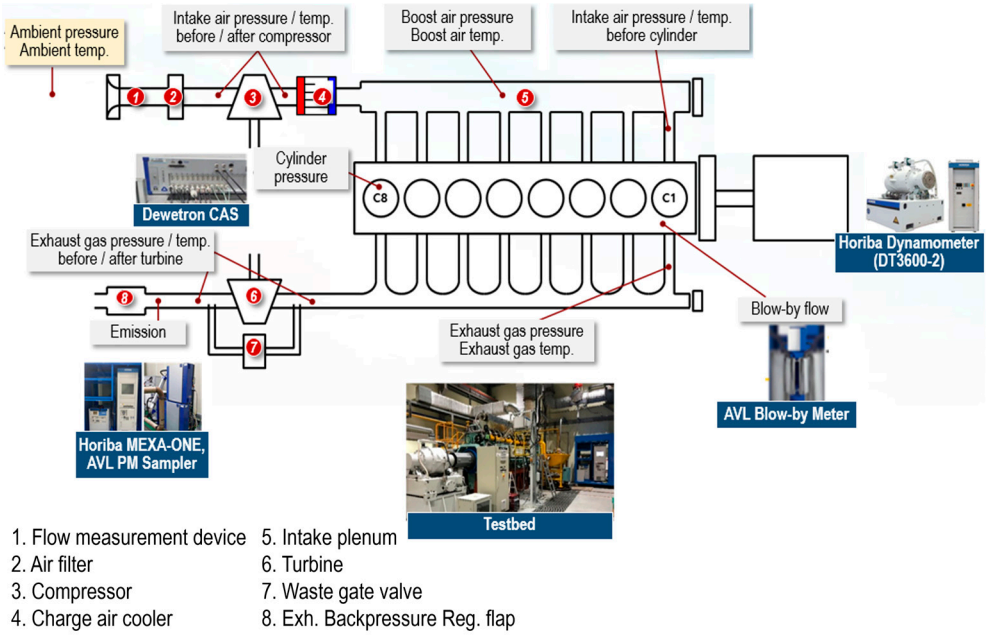

Figure 1. schematic representation of the engine setup.

2.2. Prechamber and Engine Geometry

Fig.2 shows detail description of engine geometries with prechamber. As shown in Fig.2, the larger of the chambers (main chamber) is the conventional SI combustion chamber, while the smaller one, having a fixed volume(prechamber), is where combustion is initiated by the spark plug. The pre-chamber volume is 1,745 mm^3 (0.107 in^3), accounting for approximately 1.76% of the engine's clearance volume, with 1.85% of the total injected fuel delivered to the pre-chamber through the auxiliary pre-chamber injection orifice. The illustration within the boxed area at the top of Figure 2 represents the two cross-section utilized for analysis in this study. The figure depicts the physical phenomena occurring within the PCSI engine at two different cross-sections.

Previous studies have reported that the optimal pre-chamber volume ratio ranges from 2.4% [23] to 3.5% [18], considering the trade-off between ignition energy and NOx emissions. The investigated numerical and experimental test ranges in these studies span 2.0% to 3.5% [3,19,23,26].

In comparison, the pre-chamber volume of the target engine in this study is relatively small. This design choice is based on the premise that reducing pre-chamber volume in PCSI engines enhances ignition stability and combustion speed, thereby improving lean-burn operation and thermal efficiency.

 doi:10.20944/preprints202503.0200.v1

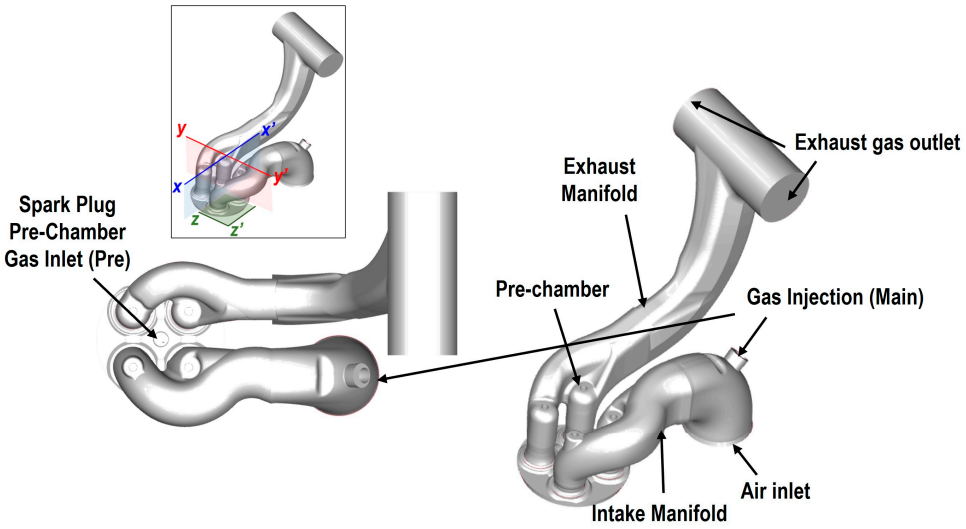

Figure 2. CAD surface data of the pre-chamber and combustion chamber design including the intake and exhaust ports geometry.

3. Numerical Model

Numerical simulations are performed using the commercial CFD code, Fire by AVL [34], a computational fluid dynamics software for computing compressible three-dimensional, chemically reacting flows in complex geometries with moving boundaries. Using this software, the full engine processes can be simulated by a movable mesh model during the engine cycle process.

3.1. Computational Mesh

Figure 3 shows the computational domain created from the real engine geometry, including the intake/exhaust ports and the pre-chamber. As can be seen the pre-chamber is aligned with respect to the cylinder axis. Polyhedral meshing was used for the whole computational domain with a base cell size of 4 mm.

In the pre-chamber region, the cell size was fixed to 1.8 mm and 1.3 mm for cells located close to the walls. Moreover, Piston Displacement Function (PDF) was used to improve grid resolution. o

Total number of grids count ranged from 0.987 to 1.556 million, with time steps controlled via CFL conditions. The mesh type of grid system consists of tetrahedron elements (0.64%), hexahedron elements (0.6%), pyramid elements (3.25%) and polyhedron elements (95.51%). At the time of ignition +13.41 deg CA additional spherical refinement is applied in spark plug area. Relatively fine mesh in pre-chamber needs to be generated to resolve flow field properly and transfer channels(orifice) between PC and main chamber have to be refined with at least 8 cells in between. Refinement of connecting channels is extruded into main chamber (cone or cylinder refinement) in the direction of flame jets. Finally, the mesh was refined to 0.5 mm at the spark gap location where all geometric details are captured, a few cells between electrodes to better capture the initial flame kernel and the early combustion evolution.

 doi:10.20944/preprints202503.0200.v1

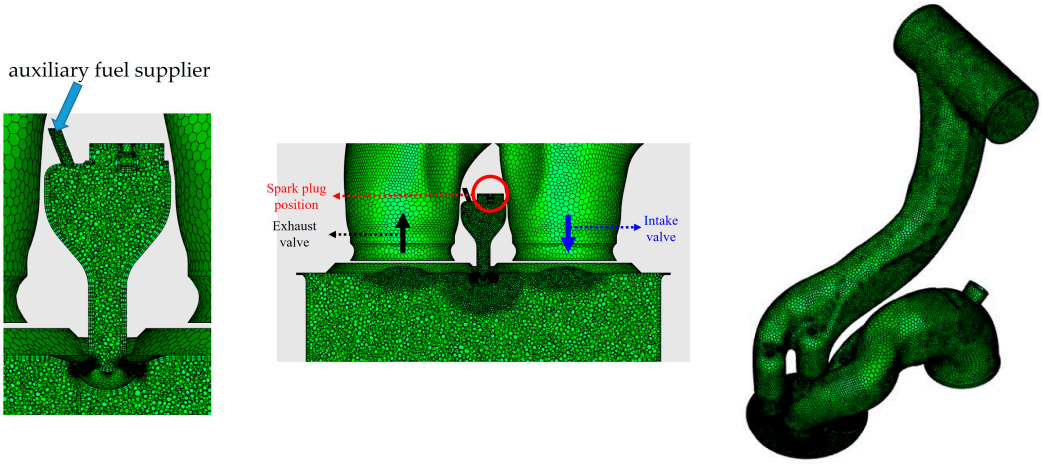

(**a**) Sectional zoomed view of prechamber computational grids (**b**) Whole computational grids @TDC

Figure 3. Computational mesh details for prechamber and main engine simulations.

3.2. Description of Test Geometries

This study investigates the effects of pre-chamber diameter, volume, and cone angle on scavenging performance, chemical composition variations, and emissions using the previously described CFD model. The pre-chamber cone angle is set to 130° and 140°, as illustrated in Fig. 4. Specifically, the analysis examines two pre-chamber diameters, two kinds of volume configurations, and two cone angles, as detailed in Figure 5 (Cases 1–3). For each pre-chamber configuration, the nozzle area ratio, denoted as β, is mathematically defined as the ratio of the total nozzle exit area to the pre-chamber volume, as expressed in Equation (1). This parameter, representing the relative flow area of the orifices and the penetration of the flame jet, was systematically varied to evaluate its impact on combustion characteristics [3,19]. In fluid dynamics, non-dimensional parameters such as β allow for generalization and scalability, enabling comparisons across different engine geometries and operating conditions.

$$\beta = B \cdot \frac{A_t}{V_{pcc}} \quad (1)$$

where, B is cylinder bore, A_t total flow area of all pre-chamber orifices and V_{pcc} is pre-chamber volume.

Numerous previous studies [3,18,19,23,26] have aimed to optimize pre-chamber geometry by determining the optimal β parameter value, as β primarily governs the flow characteristics of flame jets propagating from the pre-chamber into the main chamber. In this study, the β parameter value ranges from 0.03 to 0.034. In this study, the β parameter ranges from 0.03 to 0.034—well below the 0.2~0.4 range found in previous work—indicating a relatively larger orifice diameter compared to the pre-chamber volume. While previous studies reported that β = 0.3 optimizes combustion stability and emissions, our engine was designed with a smaller pre-chamber to improve cold-start performance and reduce in-cylinder flow interference. Therefore, we applied the optimal orifice diameter range of 1.8–2.0 mm [3,18,19,23] on a reduced-volume pre-chamber.

The total number of nozzles in the pre-chamber was set to eight, ensuring a well-distributed spatial arrangement of the igniting jets ejected from the pre-chamber. Noteworthy feature of this study compares the combustion characteristics of orifice and diverging-tapered-hole pre-chamber nozzles to analyze the underlying mechanisms and evaluate the potential advantages of the diverging-tapered-hole nozzle for PCSI engine applications (Figure 5, Case 4).

Unlike conventional orifice, the diverging-tapered-hole nozzle minimizes flow separation at the nozzle exit, facilitating more uniform air-fuel mixing. As a result, it generates stronger turbulent jets, which enhance main-chamber ignition and improve combustion stability, particularly under ultra-lean operating conditions.

A critical parameter that has not been extensively analyzed in previous studies is the pre-chamber cone angle, as schematically illustrated in Figure 4. Most prior research has employed a cone angle of 130° [23] or 140° [35]. However, in Miller cycle engines—such as the one examined in this

 doi:10.20944/preprints202503.0200.v1

study—where early intake valve closing (EIVC) extends the com-pression stroke, variations in the cone angle may have a significant impact on scavenging performance. Additionally, the volume ratio of the pre-chamber to the main chamber is 1.31% for Cases 1 and 2, and 1.38% for Cases 3 and 4.

Furthermore, as the turbulent jet flows through the pre-chamber orifice, it interacts with flow resistance, potentially influencing the composition and concentration of active intermediate radicals within both the cold jet and the initial jet flame. Given these potential effects, this study systematically investigates the influence of cone angle variations on the combustion and emissions characteristics of PCSI engines, as shown in Figure 4.

Figure 5 illustrates the four geometric configurations analyzed in this study, detailing the key dimensional parameters alongside the three-dimensional computational mesh representation.

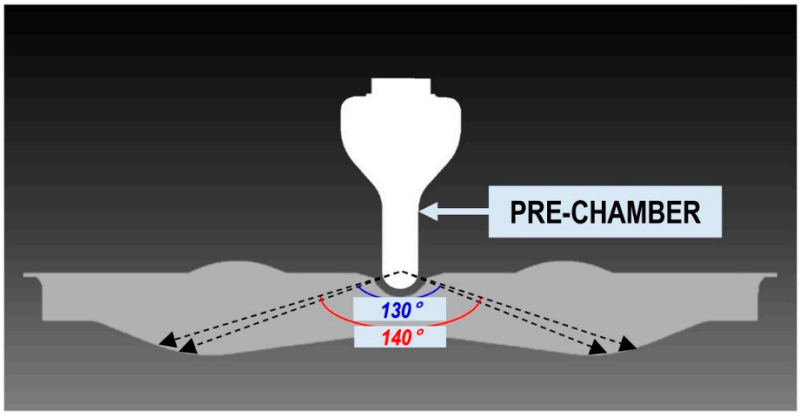

Figure 4. Cross-sectional illustration of the combustion chamber and pre-chamber installation with different cone angles.

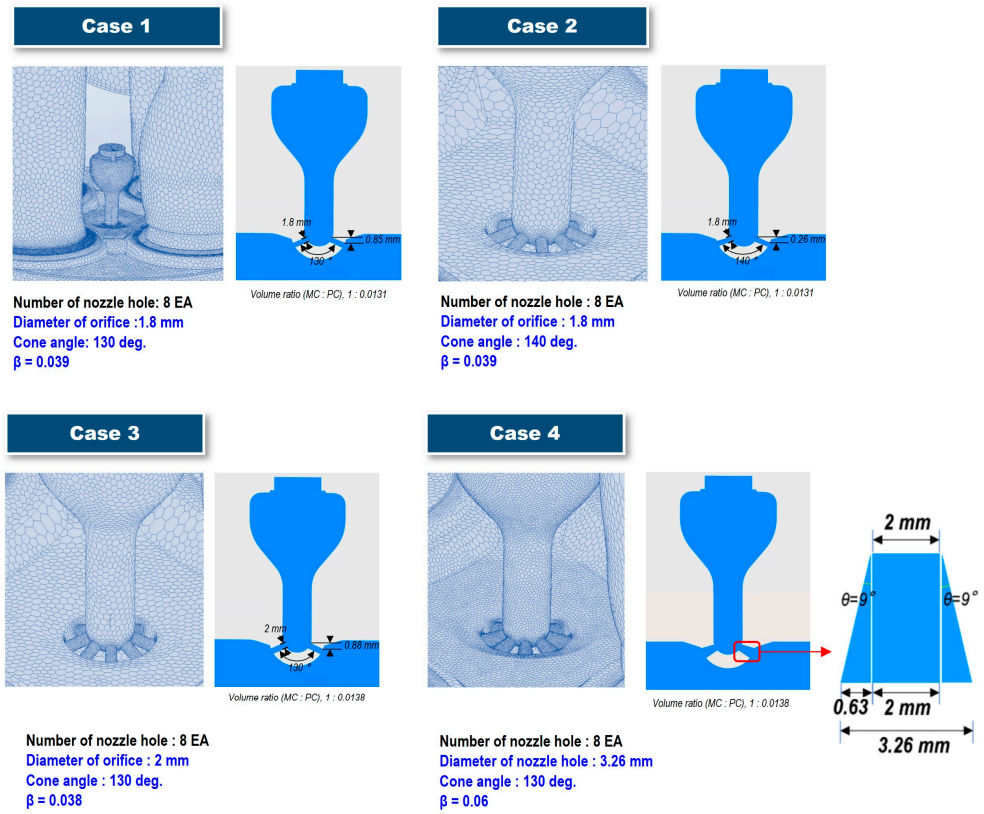

Figure 5. Schematic diagram of test cases with computational mesh of the fluid region in the prechamber.

 doi:10.20944/preprints202503.0200.v1

3.3. Turbulence Model

In this study, a k-ζ-f model [35] was chosen as the turbulence model because of its high accuracy and convergence stability, which has been optimized from the near-wall turbulence closure model proposed by Durbin [36]. This is another version of low-Re turbulence model. In addition to the turbulent kinetic energy and its dissipation rate in the standard k-ε turbulence model, the wall-normal velocity fluctuation v^2 and its source term f are introduced as variables to incorporate near-wall turbulence anisotropy as well as non-local pressure-strain effects. The need for damping functions can be avoided by careful introduction of this kind of relaxation [37]. This model enhances numerical stability of the original v^2-f model by solving a transport equation for the velocity scale ratio $\zeta=v^2/k$ as oppose to the velocity scale v^2. Thus, to consider the non-isotropic turbulence which occurs in-cylinder flow, it is expected that the k-ζ-f model has the much better prediction capability compared to the k-ε model. It was also reported that the k-ζ-f model shows better predictive ability in many engineering problems than the conventional k-ε turbulence models [28]. All the walls of the computational domain are set as isothermal from experimental da-ta. Hybrid wall treatment [34] was employed to describe the behavior of the fluid in wall boundary layers. The decision to employ a hybrid wall treatment was driven by computational efficiency and the specific requirements of the simulation. While the hybrid wall treatment in FIRE code [34] allows for coarser near-wall meshing, its application to the k-ζ-f turbulence model may lead to a slight reduction in accuracy when resolving detailed near-wall turbulence effects. However, by using a relatively larger mesh size in the main chamber—except for the near-wall regions inside the pre-chamber—and applying a wall function approach, the computational cost was significantly reduced while effectively leveraging the high accuracy of the k-ζ-f model.

3.4. Combustion Model

Turbulent Jet Ignition (TJI) in lean-burn engines presents significant challenges for combustion modeling. While pre-chamber combustion resembles that of a conventional SI engine, ignition in the main chamber—driven by turbulent hot jets—differs fundamentally from traditional premixed flame propagation. To address this complexity, the Extended Coherent Flamelet Model (ECFM-3Z) was selected for its capability to model both premixed and diffusion combustion.

ECFM-3Z tracks flame propagation through a transport equation for flame surface density (Σ), incorporating convection, diffusion, turbulent stretch, thermal expansion, and mean flow effects. As this transport equation has been extensively detailed in previous studies [14,39], it is omitted here for brevity.

The equation consists of two source terms: one is source term which represents flame surface density generation, primarily influenced by turbulent net flame stretch, which depends on turbulence intensity, velocity gradients, and length scales, with corrections for curvature and thermal expansion under the assumption of isotropic flame distribution. The other is sink term which accounts for local flame extinction due to unfavorable conditions such as excessive strain, heat loss, or insufficient reactants.

These terms are mathematically expressed in Equation (2).

$$S_{source} = \alpha K_{eff} \Sigma \quad and \quad S_{sink} = \beta \frac{\rho_{fu,fr} S_L}{\rho_{fu}} \Sigma^2 \tag{2}$$

In this equation $\varrho_{fu,fr}$ is the partial fuel density of the fresh gas, ϱ_{fu} the density of the fresh gas and S_L is laminar flame speed.

Here,

$$K_{eff} = K_t = \frac{\varepsilon}{k} C_t \tag{3}$$

K_t is critical property since it influences the source term for the flame surface and therefore, the mean turbulent reaction rate. From Equation (3), it can be observed that flame stretch is expressed as the large-scale characteristic strain, ε/k, modified by a correction function, C_t, which accounts for turbulence scale size, viscous effects, and transient behavior[40]. The parameter C_t is a function of turbulence parameters and laminar flame characteristics [34].

 doi:10.20944/preprints202503.0200.v1

The coefficients α the stretch factor, and β in Equation (1) are arbitrary tuning constants used in ECFM-3Z.

The ECFM-3Z model divides combustion into three zones—fuel, air, and air-fuel mixture—with mixing governed by a characteristic time scale derived from the k-ζ-f turbulence model. Burnt gas properties are determined using the reaction progress variable, while an auto-ignition model estimates ignition delay based on reaction time scales. Although ECFM-3Z lacks detailed chemistry, it effectively models turbulent premixed flame propagation, making it well-suited for SI engine combustion simulations [41].

The model requires laminar flame speeds, which depend on local pressure, fresh gas temperature, and unburned fuel-air equivalence ratio. Empirical correlations, such as Metghalchi and Keck [42], often underpredict laminar flame speeds under real engine operating conditions [41]. To enhance accuracy, this study utilizes pre-tabulated values from AVL FIRE, generated using detailed reaction mechanisms. Laminar flame thickness is computed from the temperature profile normal to the flame front and the chemical time, which is derived from the characteristic time of laminar flame propagation using the Zeldovich Number, dependent on the activation temperature of fuel oxidation. While ECFM-3Z does not incorporate detailed chemistry, it solves transport equations for the mean concentrations of key chemical species, including O_2, N_2, CO_2, CO, H_2, H_2O, O, H, N, OH, and NO, where "mean concentrations" refer to the global averages across all three mixing zones within a computational cell.

A spherical model is employed for pre-chamber ignition, coupled with ECFM-3Z. The spherical flame kernel forms at the spark plug gap, based on spark position, ignition timing, flame kernel radius, and spark duration. Ignition begins at -14 CA BTDC, with ignition energy calculated from flame kernel radius and thermodynamic properties. The flame surface density remains constant in all ignition cells within the kernel radius for the spark duration and must be self-sustaining for propagating combustion post-ignition. For further details on the combustion simulation methodology, refer to [34].

3.5. Turbulence-Chemistry Interaction

The interaction between turbulence and combustion chemistry is critical in PCSI applications, as turbulent reactive flow leads to mutual influences between combustion dynamics and flow characteristics. Compared to conventional SI engines, PCSI systems exhibit highly inhomogeneous turbulent flow fields, characterized by steep spatial gradients at jet boundaries and rapid temporal evolution. As the flame front propagates, it interacts with both large and small eddies, enhancing turbulent mixing and intensifying diffusive processes within the flame structure.

As discussed in Section 3.2, the Flame Surface Density (FSD) transport equation includes source and sink terms that account for flame stretching and quenching effects, essential for accurately modeling flame front dynamics under both laminar and turbulent conditions. The ITNFS (Intermittent Turbulence Net Flame Stretch) model [43] is used to simulate the interaction between individual vortices and flame fronts via direct numerical simulation (DNS). It assumes that each turbulence scale independently influences flame stretching, with the cumulative effect inferred from individual scale behavior in fully turbulent flow. However, in real PCSI engines, flame behavior is inherently anisotropic, making the assumption of isotropic turbulence invalid. As a result, the ITNFS model does not fully account for turbulence anisotropy, potentially introducing inaccuracies in combustion analysis results [14,43]. Despite these limitations, the ITNFS model was employed in this study to simulate turbulence-chemistry interactions, as no more advanced model is currently available. This selection was made to ensure computational feasibility and efficiency.

3.6. Pollutant Modeling

Pollutant modeling is conducted within the burnt gas region of the mixing zone in each computational cell. Two sets of reactions are considered: (1) reactions occurring in hot combustion products formed from unburned gases in the mixing region, and (2) reactions associated with the

 doi:10.20944/preprints202503.0200.v1

turbulent mixing of fuel and air from the burnt gas region into the mixed burnt gases. The burnt gas region contains combustion products, air, and fuel, facilitating diffusion reactions that contribute to carbon monoxide (CO) and soot formation.

The ECFM-3Z model enhances the accuracy of flame property calculations, CO equilibrium reactions [45,46], and NOx kinetics via the extended Zeldovich mechanism focusing on post-flame zones with Fenimore prompt NOx mechanism to model NOx formation in the flame front [47]. NOx formation occurs in both the flame front and post-flame gases. Hence, combining the Extended Zeldovich mechanism with Prompt NOx mechanism can significantly enhance the accuracy of NOx predictions in pre-chamber combustion engines, especially under conditions where both thermal and non-thermal NOx formation pathways are relevant. This study used the prompt NOx mechanism in the flame-front zone, where hydrocarbon radicals and N_2 interact and the extended Zeldovich Mechanism in the post-flame zone, where high temperatures drive thermal NOx formation. Finally, dynamically link these zones using temperature, equivalence ratio, and chemical species concentrations.

CO formation and its subsequent oxidation into CO_2 within the burnt gas mixing zone are modeled using a six-step reduced kinetic mechanism (CORK – CO Reduced Kinetics) [45]. This CORK model improves upon the four-step mechanism [45] by incorporating two additional reactions for C_2H_2 and C_2H_4 [46].

3.7. Initial and Boundary Conditions from Experiment and 0D/1D Simulation

3.7.1. Experimental Data for Initial and Boundary Conditions

At the inlet and outlet boundaries, constant total pressure and temperature obtained from experimental measurements (Table 2) are applied. The species concentrations are prescribed to maintain a global air-fuel equivalence ratio ($\lambda = 2$), with air modeled as a mixture of N_2 (77%) and O_2 (23%). Additionally, the fuel injection profiles into both the pre-chamber and main chamber, along with fuel temperature, were experimentally measured and applied to the simulation. Uniform pressure and temperature distributions were set as initial conditions, reflecting the average operating conditions of experimental engines. In the cylinder and pre-chamber, initialization is performed using experimentally measured pressure values and appropriate temperature conditions to ensure consistency with physical boundary conditions and thermodynamic states.

3.7.2. 0D/1D Simulation for Initial and Boundary Conditions

Some of the boundary conditions for the 3D simulations were obtained from a 0D/1D simulation model, which was developed in-house for the baseline engine. This model incorporates a one-dimensional wave action model [47,48] for the intake and exhaust pipes, a thermal networking heat transfer model [47,49] for calculating heat transfer between engine components, and a thermodynamic model for in-cylinder combustion and gas exchange processes. In this in-house simulation code, the intake and exhaust systems, including cylinders and junctions, are represented using a one-dimensional or quasi-dimensional approach based on gas dynamics simulation techniques. The components (e.g., throttle body, turbocharger, compressor, throttle body, plenum, muffler) connected to the engine's intake and exhaust system were thermodynamically modeled. These simulations employ the non-isentropic formulation of the method of characteristics [48] to accurately capture flow behavior. During the compression, combustion, and expansion phases, the combustion heat release rate is governed by an energy balance equation, which is defined using experimentally measured heat release profiles.

Another component of this code is the heat transfer analysis, which is performed to calculate the temperatures of engine components, including the cylinder walls, piston, head, and exhaust valves. This analysis employs the thermal-network method [49,50] to predict component temperatures based on engine operating conditions such as speed, load, and pressure. Thermal network methods are

 doi:10.20944/preprints202503.0200.v1

widely used to predict the temperatures of engine components, including the piston, cylinder head, and liner. These methods simplify complex heat transfer phenomena by representing them as manageable resistive and conductive networks, where heat transfer is modeled similarly to an electrical circuit. In this approach, nodes correspond to key engine components (e.g., piston crown, cylinder head, exhaust valve and liner), with thermal resistances representing conduction and convection pathways within the system. The temperature at each node is computed using linear equation-solving techniques, such as the Gauss elimination method. The output provides the final temperature of each component and the energy flow along different heat transfer pathways. In this program, boundary conditions are defined using experimentally measured coolant and oil temperatures for nodes exposed to these fluids.

The computational flowchart of the in-house code used in this study is presented in Figure 6. As shown in the flow chart, the simulation initializes by loading input/output files and setting engine parameters. It applies the method of characteristics for 1D pulsating flow in intake/exhaust pipes and imports experimental heat release rate data for accuracy. Operating conditions are defined, and energy balance equations integrate flow, combustion, and heat transfer data. The model computes component temperatures, performs gas exchange and heat transfer calculations, and determines cylinder volume variations. Finally, it outputs temperatures, heat flows, and flow efficiency metrics, concluding the simulation. The 0D/1D simulation was first executed for seven or eight cycles until the convergent criterion had been satisfied. It was considered that the solution reached periodicity if the difference between volumetric efficiency of the first cylinder in the previous cycle and that of present cycle is less than 0.01. The converged solutions would be used as initial data and boundary conditions for solid surface temperatures of cylinder head, liner, piston, pre-chamber and spark plug.

The model was validated using available experimental data, as shown in Figure 7, where the intake and exhaust pressure trends are compared. As shown in Figure 7(a), the simulation accurately captures pressure waveforms from compression and expansion wave interactions due to piston movement, even in the complex turbocharged V8 engine. Figure 7(b) shows a strong match between simulation and experimental exhaust pressure waveforms, successfully predicting compression waves during the power stroke. This validated 0D/1D model was used to determine boundary conditions in hard-to-measure areas, such as the piston and liner surfaces temperatures.

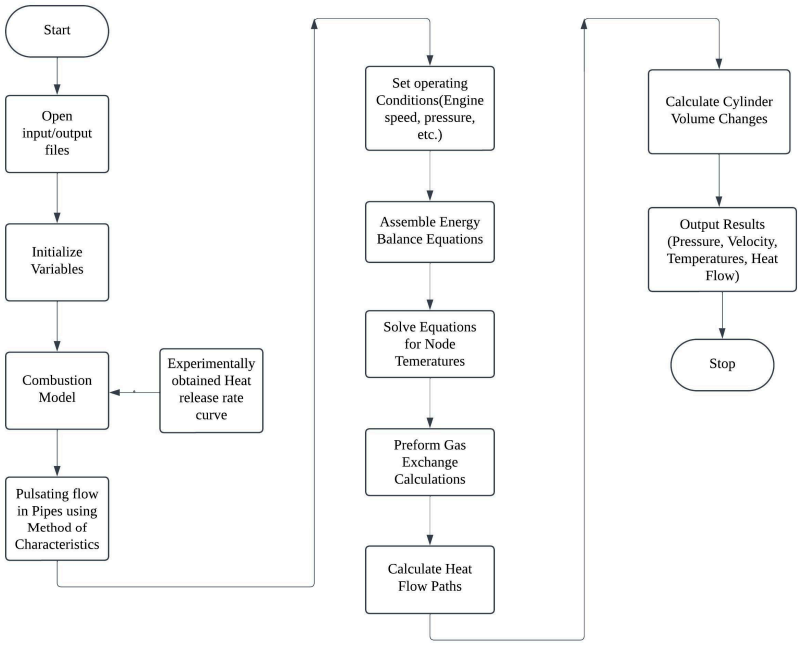

Figure 6. Computational flowchart of the 0D/1D Program used in this Study.

 doi:10.20944/preprints202503.0200.v1

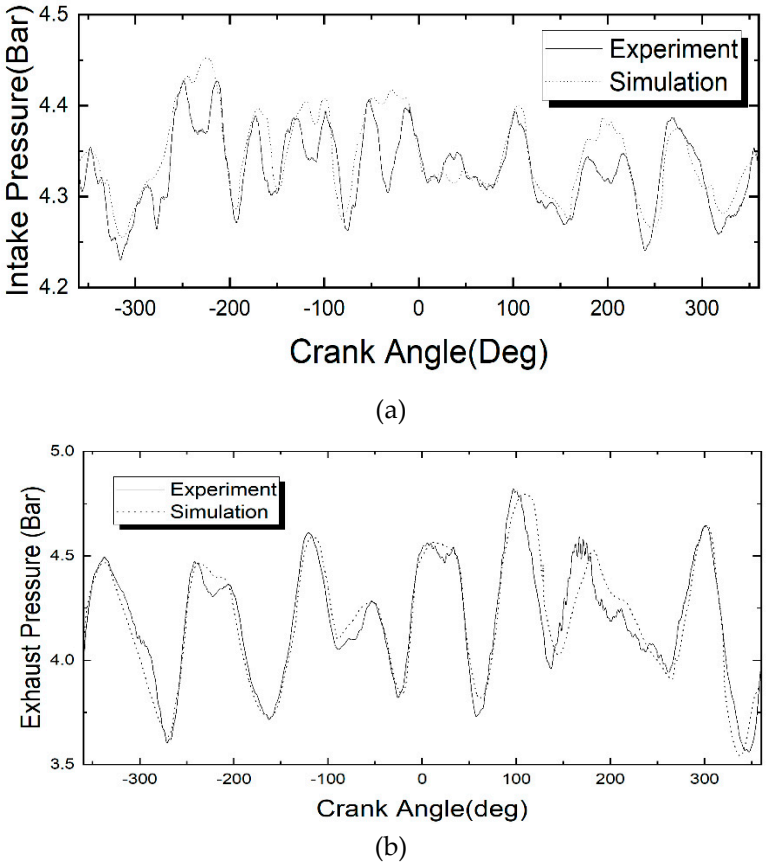

Figure 7. Comparison of pressure measurements with 0D/1D simulation results for (a) the intake duct and (b) the exhaust duct.

3.8. Simulation Control Setting

In particular, in the present work, the Reynolds averaged Navier-Stokes equations have been solved by using SIMPLE (Semi-Implicit Method for Pressure-Linked Equations) algorithm and a second-order upwind TVD (Total Variation Diminishing) scheme with Roe's MINMOD limiter with a blending factor 0.5 is selected to discretize convective terms for momentum equation and upwind schemes for turbulence and energy equations. Crank-Nicolson time integration is used for time discretization and the CFL (Courant Friedrichs Lewy) number for time step size is in ranging from 0.05 to 0.1. The solution is iterated until the convergence criteria are achieved. In general, it is observed that the residual for the momentum equations, the turbulent kinetic energy and turbulent energy dissipation rate are below 10^{-4}. The energy equation residual is well below 10^{-5}, while the residual for the continuity equation is below 10^{-4}. The simulation period should extend through the full engine cycle to accurately capture realistic combustion and exhaust processes, as the intake, compression, and exhaust phases significantly influence prechamber performance, which in turn affects combustion and emissions in lean-burn engines. However, most recent CFD studies on PCSI engines simulate only the closed cycle (from intake valve closing (IVC) to exhaust valve opening (EVO)) due to computational resource limitations and the high numerical complexity involved [29,41]. This study simulates a full 720° crank angle (CA) engine cycle, spanning from the exhaust valve opening (EVO) of the previous cycle to the EVO of the current cycle, encompassing all critical engine processes.

In internal combustion engine (ICE) development, 3D-CFD simulations are commonly employed to study stationary operating points. However, previous research has demonstrated that even for steady-state conditions, multiple consecutive cycles are required to obtain a statistically representative solution [50]. Literature suggests that at least three consecutive cycles should be simulated to minimize uncertainties associated with initial conditions and enhance solution stability

 doi:10.20944/preprints202503.0200.v1

[51], though this approach significantly increases computational cost. To address this, the present study employs three consecutive engine cycles for each operating condition to ensure numerical convergence and reduce the dependency on assumed initial conditions. The Algebraic Multi-Grid (AMG) solver is utilized as the linear system solver, where matrix coefficients are strategically aggregated to construct a coarser grid representation, eliminating the need for additional discretization while maintaining computational efficiency.

Simulations are run in parallel on a distributed memory cluster of Intel Xeon W-2265@3.5GHz computer with processor consisting of 32 cores and 192 GB of DDR4 2933 memory per node. About 504 hours were needed to run a 3-cycle fired simulation for one case.

4. Results

This section may be divided by subheadings. It should provide a concise and precise description of the experimental results, their interpretation, as well as the experimental conclusions that can be drawn.

4.1. Calibration of Combustion Model

As previously mentioned, ECFM-3Z is a combustion model adopted in this study to simulate complex combustion processes in internal combustion engines. A critical parameter in this model is the stretch factor, presented in Equation (2), which plays a significant role in accurately predicting flame behavior under various operating conditions.

Several previous studies have attempted to optimize this parameter to overcome the limitations of flamelet-based models [27,39]. However, no research has been reported on its application to active-type natural gas fueled pre-chamber combustion systems. Therefore, this study aims to tune the ECFM-3Z model by systematically varying the stretch factor across a wide range. Specifically, the stretch factor was adjusted from 0.3 to 0.77, and an empirical correlation proposed in recent studies [14,52], as given in Equation (4), was applied. This correlation expresses the stretch factor in ECFM-3Z as a function of the flame-based Karlovitz number, based on the principle that the stretch factor modulates the interaction between turbulence and the flame front, influencing flame propagation speed and stability.

$$\beta = G^{G\_Exp}, G\_{Exp} = 2.0 \quad (4)$$

where, $G = \sqrt{-0.5\tanh\left(C_{k,1} log_{10}(Ka_t) - C_{k,2}\right) + 0.5}$, $C_{k,1} = 1.3, C_{k,2} = 2.1$

The flame-based Karlovitz number included in Equation (5) is calculated using the following equation.

$$Ka_t = \frac{\delta_L / S_L}{(\nu/\varepsilon)^{1/2}} \quad (5)$$

where, δ_L represents laminar flame thickness, S_L is laminar flame speed, ν denotes kinematic viscosity and ε is turbulent dissipation rate.

Figure 11 presents the heat release rate as a function of crank angle degrees for various stretch factor($\boldsymbol{\alpha}$) values, comparing the simulation results with those derived from experimentally measured in-cylinder pressure data of case 3. In Figure 8, SF represents the stretch factor, while SF_opt denotes the stretch factor calculated using Equation (4).

 doi:10.20944/preprints202503.0200.v1

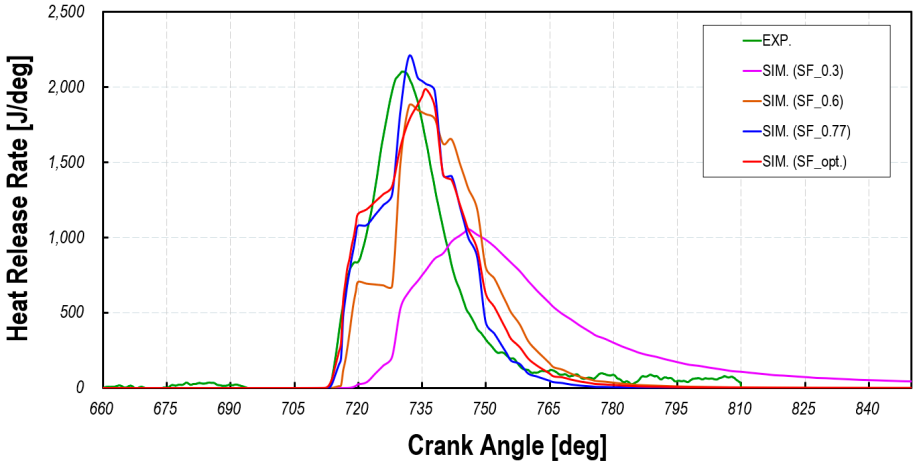

Figure 8. Heat release rate versus crank angle degrees for different α values, in comparison with experimental apparent heat release.

Figure 8 presents the heat release rate as a function of crank angle degrees for various α values, comparing the simulation results with those derived from experimental in-cylinder pressure measurements for Case 3. The experimental data in this figure represents the apparent heat release rate. The results indicate that as α increases, both the heat release rate and its rate of change increase, demonstrating that higher α values correspond to an increase in combustion speed. Another noteworthy feature of the results in Figure 8 is that, despite extensive model tuning, the observed delayed combustion phasing indicates significant inaccuracies in the current turbulence-flame interaction model, which fails to accurately represent the anisotropic characteristics of turbulent flames in PCSI engines. In PCSI combustion, the formation of strong turbulent jets leads to the rapid dissipation of turbulent kinetic energy (TKE), posing a major challenge in modeling turbulence-flame interactions. Consequently, the flame does not have sufficient time to adjust to the turbulent flow field, resulting in numerical predictions that deviate from actual combustion behavior.

Figure 9 illustrates the effect of stretch factor variations on combustion speed by dividing the combustion duration into three phases: 10% mass fuel burn duration (MFB10), 50% mass fuel burn duration (MFB50), and 90% mass fuel burn duration (MFB90). As observed in the figure, higher α values correspond to faster combustion rates, leading to a reduction in burn duration. Additionally, in the SF_opt case, where the flame-based Karlovitz number is considered based on PCSI engine multi-mode combustion, a high prediction accuracy is achieved for the flame development angle (MFB10) to MFB50 region. These results indicate that tuning the stretch factor using Equation (4) provides the highest prediction accuracy, while using a single stretch factor shows that the optimal range is $0.6 < \alpha < 0.77$. This range deviates from the previously proposed optimal value ($\alpha = 0.525 – 0.6$) suggested in earlier studies [39]. Thus, it is confirmed that the correction of the stretch factor in ECFM-3Z must be performed individually based on engine operating conditions, fuel type, and combustion strategy. Based on these results, all CFD simulations in this study were conducted using the stretch factor calculated from the correlation in Equation (4), which demonstrated the highest accuracy in combustion analysis.

 doi:10.20944/preprints202503.0200.v1

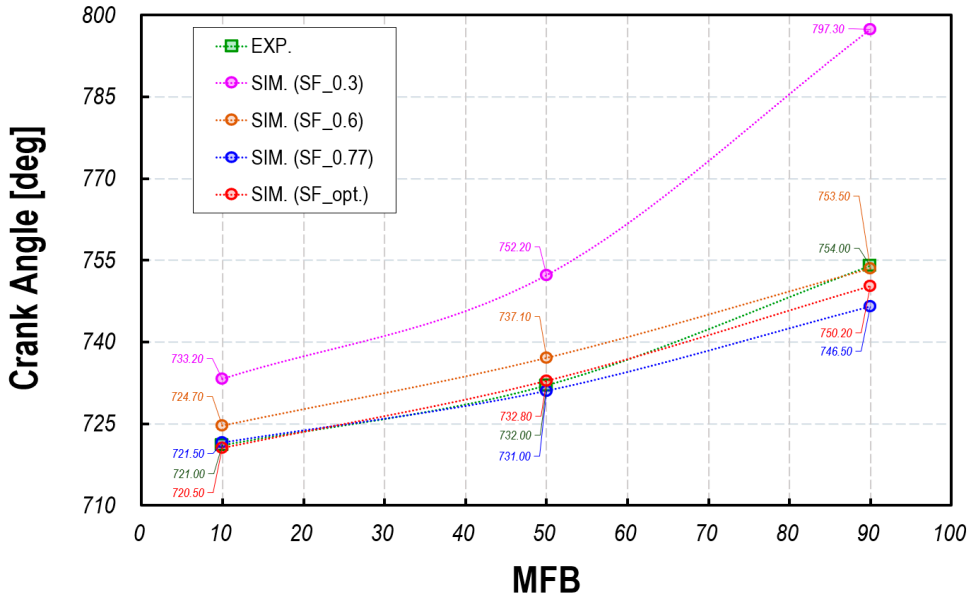

Figure 9. Mass burned fraction versus crank angle degrees for different α values, in comparison with MBF calculated based on experiment.

4.2. Validation of CFD Simulation with Flamelet-Based Combustion Model

Before analyzing PCSI combustion engine using CFD, validating the CFD model is a crucial initial step to ensure the accuracy and reliability of the numerical solution. For this purpose, the operating point described in Table 2 was selected. The in-cylinder pressure and emissions were compared with experimental measurements from the 8-cylinder engine, considering the pre-chamber configuration of Case 3. The validation test was conducted at an engine speed of 1000 rpm, under full-load, ultra-lean conditions (λ = 2).

Figure 10 shows the comparisons between prediction and measurement for pressure trace of in-cylinder and pre-chamber at 1000rpm, full load. The experimental measurements encompass 300 cycles of pressure data with an associated average value, while the CFD simulation reports the average cylinder pressure computed from three cycles. It can be observed from Figure 6 that the predicted pressures are reasonably good agreement with the experimental data. The close agreement between the in-cylinder pressure traces and the experimental data is attributed to the precise tuning of the stretch factor in the ECFM-3Z model, as previously discussed.

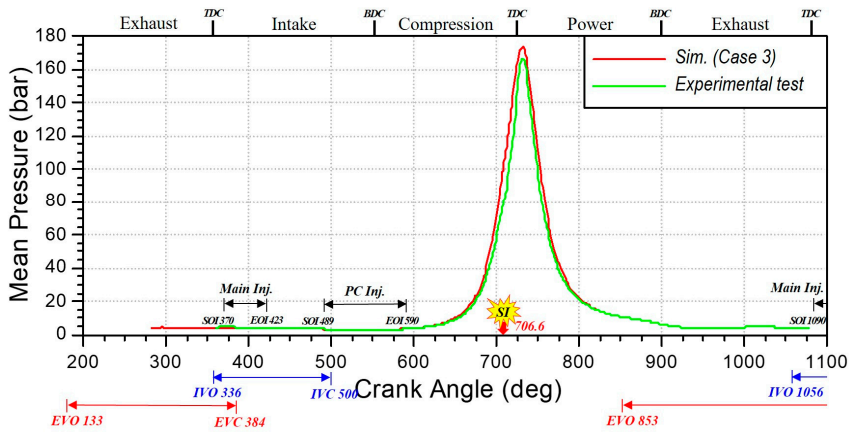

(a) In-main chamber pressure trace

 doi:10.20944/preprints202503.0200.v1

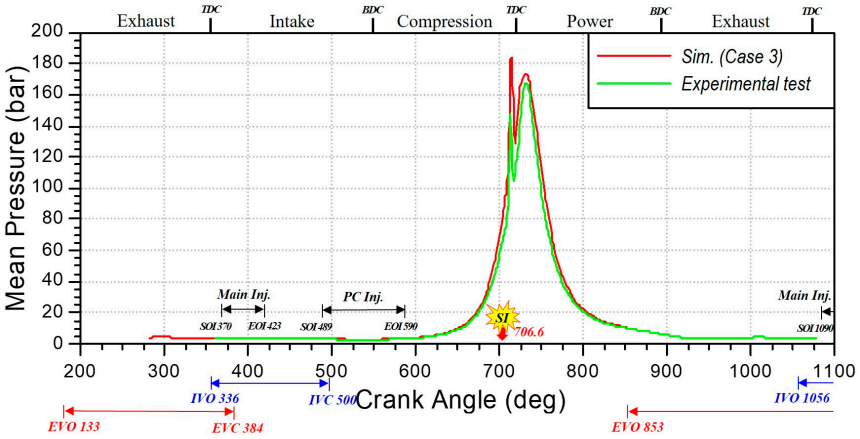

(b)In pre-chamber pressure trace

Figure 10. Comparisons of in-main chamber and in-pre-chamber pressure between measurements and predictions.

Further validations on the emissions of CO and NOx were indicated in Figure 11. The CFD simulation results for CO emissions show an overprediction of approximately 11% compared to the experimental values. However, there exist large discrepancies of NO emission between the simulation and experiment. It can be found from Figure 6 that the predicted NOx emissions are 24.7% larger than the meas-ured value. This is may be due to the problems that combustion sub-models may cause some numerical error resulting in overestimating pressure and temperature in pre-chamber. This is because in lean combustion conditions, using the Zel'dovich Mechanism for NOx prediction may lead to overestimation. This is primarily due to the inherent limitations of the mechanism and the characteristics of lean combustion. The Zel'dovich mechanism describes the formation of thermal NO, which predominantly occurs at high temperatures (>1800 K); however, in lean combustion, the combustion temperature decreases, limiting high-temperature regions, and consequently, actual NOx production may be lower than the predictions made by the Zel'dovich mechanism, which is highly sensitive to temperature and reaction rate constants, potentially leading to an overestimation of NOx formation at elevated temperatures. Additionally, the overestimation of NOx emissions can be attributed to the increased oxygen concentration. While a relatively high oxygen concentration is present, the low temperature and short residence time significantly suppress NOx formation. However, CFD models may not fully account for the effects of these ultra-lean conditions, potentially leading to an overestimation of NOx emissions. That is, in pre-chamber combustion, rapid flame propagation and high turbulence may reduce the residence time for thermal NOx formation, resulting in deviations from predicted values. The inability of the ECFM-3Z combustion model to accurately predict turbulence and mixing effects within the PCSI engine is another contributing factor to the overestimation. In pre-chamber engines, rapid mixing and flame jet dynamics can induce local temperature variations that are not fully captured by over-simplified models.

To improve the predictive accuracy of NOx emissions in PCSI engines using the Extended Zeldovich Mechanism, it is essential to incorporate the N_2O Pathway, a key NOx formation route under lean-burn conditions. Additionally, the temperature dependency of the mechanism should be modified to account for the sharp decline in thermal NOx reaction rates, and low-temperature NOx formation pathways, such as NO production from hydrocarbon radicals, must be introduced. Beyond refining the chemical mechanism, PCSI engine-specific effects should be integrated into NOx modeling by dynamically coupling local equivalence ratios and stratification, as computed from the ECFM-3Z model, with the Extended Zeldovich Mechanism.

Finally, accurately capturing turbulence effects on flame structure and reaction zones necessitates the development of numerical models that couple the Zeldovich mechanism with

 doi:10.20944/preprints202503.0200.v1

turbulence modeling, enabling better resolution of lean combustion conditions. Advancing such computational frameworks is critical for improving NOx emission predictions in PCSI engines.

For CO emissions, the ECFM-3Z model may overestimate CO levels under certain conditions due to its treatment of post-flame oxidation and turbulence-chemistry interactions. In active PCSI engines, a significant portion of CO undergoes oxidation after the main flame has passed, driven by the presence of residual radicals (·OH, O·, H·) and bulk turbulence effects. Since ECFM-3Z assumes an equilibrium-driven post-flame oxidation model, it may underpredict CO oxidation rates, resulting in higher predicted CO emissions compared to experimental values. Another factor contributing to the overestimation of CO emissions is the inadequate representation of turbulent mixing between the pre-chamber and main chamber, which affects the accuracy of CO formation and oxidation predictions. High-momentum turbulent jets enhance CO oxidation through jet-induced mixing and flame propagation acceleration; however, ECFM-3Z may not fully capture turbulence-chemistry interactions in these regions, leading to an overprediction of CO concentrations in simulations.

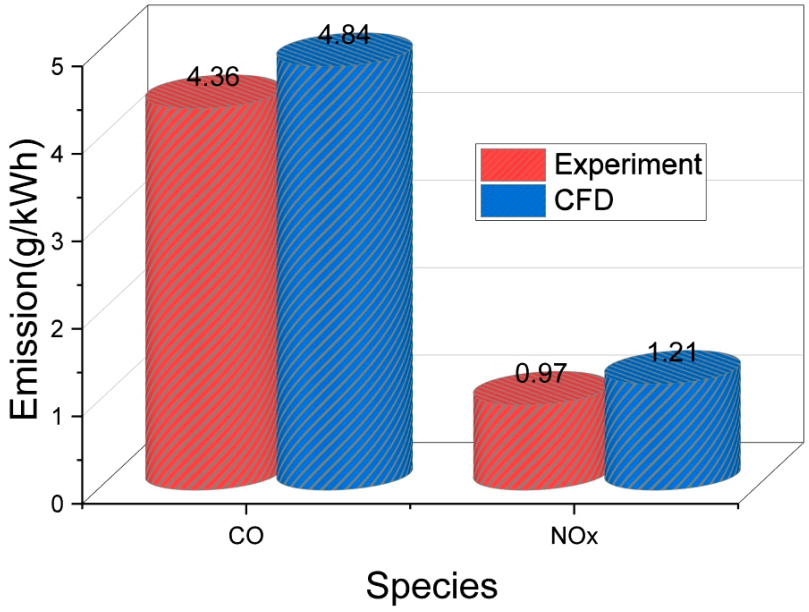

Figure 11. Experimental Validation of CO and NOx Emissions Derived from CFD Analysis.

4.3. Exploring Thermo-Fluid Interaction Between the Prechamber and Main Chamber

Figure 12 displays pressure curves for the pre-chamber (PC) and main chamber (MC) across various configurations, including a reference case without a pre-chamber (NPC). The throat diameter greatly affects the PC peak pressure—a smaller throat retains the reacting mixture longer, leading to higher pressure. In cases with a pre-chamber, the PC curve shows dual peaks: the first from rapid combustion of a near-stoichiometric mixture in the PC, and the second from the MC pressure rise propagating into the PC. The zoomed section in the upper right of Figure 12 (case 1) illustrates the interplay between the expanding flame pushing reactants out of the PC and the MC gases flowing in due to compression. When the PC pressure exceeds the MC pressure, flow reversal 1 (FR1) occurs; a later equilibrium marks flow reversal 2 (FR2). Figure 8 clearly illustrates that variations in the orifice cone angle have a pronounced effect on the pre-chamber pressure. In this study, case 2—where the cone angle was increased by 10°—produced the highest peak pressure in the pre-chamber. This outcome is likely attributable to the significant flow resistance encountered by the combusted turbulent jets as they pass through the orifices.

Table 3 summarizes these events and the residence time—defined as the interval between FR1 and FR2 [29]. Cases 1 and 2 have longer residence times due to higher flow restrictions, allowing prolonged radical dispersion but increasing the risk of chemical transformation. Shorter residence

 doi:10.20944/preprints202503.0200.v1

times indicate lower pre-chamber combustion and higher mass flow, resulting in jets richer in active species. Larger orifice diameters enable faster energy transfer to the MC, with a lower degree of pre-chamber combustion releasing more fuel energy in the MC for enhanced ignition. Case 4, which employed a diverging-tapered-hole nozzle, exhibited the shortest residence time. This is because, unlike conventional straight-hole nozzles, a diverging-tapered-hole nozzle minimizes flow separation at the nozzle exit, thereby increasing the gas jet velocity and enhancing the mixing with the air-fuel mixture in the main chamber. Previous studies [16,19,53] emphasize that excessive flow restriction may lead to recombination of active species before they effectively mix with the MC charge. As shown in Table 3, while the onset of FR1 due to combustion is nearly identical across configurations, the termination time of the discharge of high-pressure combustion products through the orifice (FR2) is strongly governed by the orifice's geometric configuration.

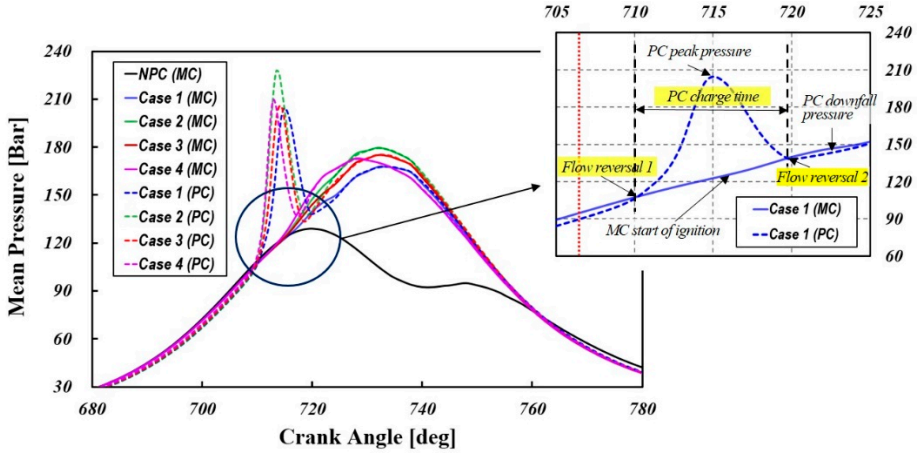

Figure 12. Pressure traces for various geometric variations in the pre and main chamber.

Table 3. Summary of flow reversal time and mixture residence time for various cases.

Cases	Case 1	Case2	Case3	Case4
FR1(P_p>P_m)	710.2	709.2	709.7	709.0
FR2(P_p<P_m)	719.2	718.4	718.1	717.2
PC residence time(deg)	9.5	9.2	8.4	8.2

Figure 13 shows the pressure differential between the PC and MC for different configurations. The results indicate that the nozzle diameter and cone angle strongly influence the PC pressure. This differential acts as the driving force for jet flame injection into the MC. Case 2 exhibits the highest peak pressure differential, while Cases 1, 3, and 4 show reductions of 25%, 22%, and 15% compared to Case 2. The elevated differential in Case 2 is likely due to higher combustion pressure in the PC. Figure 13 shows that while the onset of pressure rise in the PC is similar across different orifice geometries, the slope of the pressure rise curve varies significantly, resulting in distinct phase shifts among the cases. This variation is due to differences in the scavenging flow during compression, which affect the distribution of mixture concentration, flow velocity field, and turbulence intensity level near the spark plug. These factors influence flame propagation and speed. The peak PC pressure depends on the flow resistance encountered by the turbulent jet as it passes through the orifice. In this study, Case 2 exhibits the highest peak pressure and steepest gradient of initial rise, likely due to an optimal mixture concentration and turbulence at the ignition stage, promoting rapid flame development.

 doi:10.20944/preprints202503.0200.v1

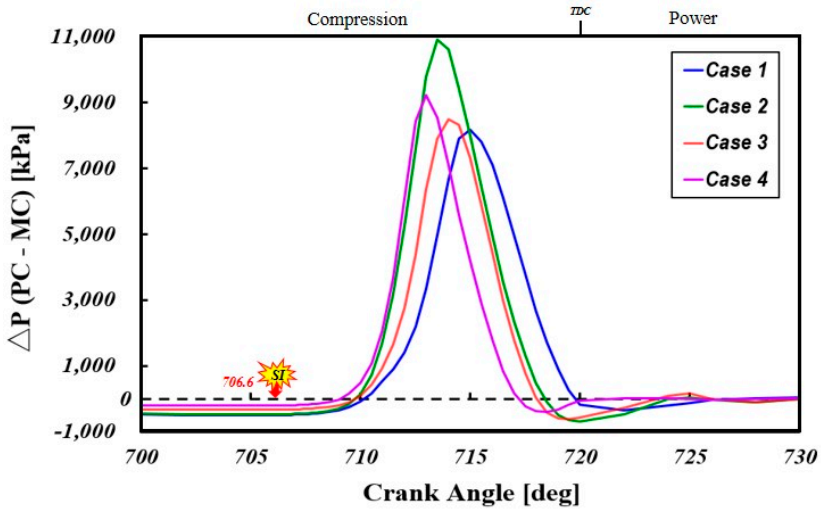

Figure 13. Temporal variations of pressure difference between pre and main chamber.

Figure 14 presents the velocity contours and flow streamlines in the pre-chamber for different cases at 706.4°CA, just before ignition. A key characteristic of the flow behavior during the compression stroke is the strong mixing of jets from each nozzle in the lower region of the pre-chamber. These mixed flows then ascend and, except for Case 2, are deflected to the left of the central axis before reaching the upper surface. The upward flow induces the formation of recirculating vortices on both the left and right sides, influencing the flow dynamics around the spark plug gap. As the upward-moving flow impacts the pre-chamber roof, it decelerates and subsequently passes through the spark plug gap. The most critical aspect of the pre-chamber flow field is the interaction and balance between the two recirculating vortices, which are primarily dictated by the nozzle jet flow rate and injection angle.

In the case of Case 4, which is equipped with a diverging-tapered nozzle, the nozzle functions as a converging-tapered-hole nozzle during the compression stroke. Consequently, the constriction in the channel induces a pressure drop, accelerating the flow and increasing the outlet velocity. This, in turn, enhances jet momentum and penetration, generating a strong, more directed upward flow toward the spark plug. As a result, a more symmetrical recirculation zone is established on both sides of the pre-chamber.

A key observation in this figure is that in Case 2, where the orifice cone angle is increased, the flow streams from the eight orifices merge in the lower region of the pre-chamber and, unlike other cases, shift rightward before ascending directly toward the spark plug. This leads to the formation of a strong and wide recirculation zone on the left side. Unlike other cases, where the right-side recirculation flow interacts with and passes through the spark plug gap, Case 2 exhibits a stagnated flow distribution. Ultimately, this result confirms that modifying the orifice cone angle has a more significant influence on the pre-chamber flow distribution at the time of ignition compared to simply altering the orifice geometry.

Figure 15(a) presents the turbulent kinetic energy (TKE) at the spark plug gap position just before ignition. Among the analyzed cases, Case 3 exhibits the highest TKE level, while Case 1 shows a 38.4% lower TKE than Case 3, Case 2 is 48.0% lower, and Case 4 is 60.2% lower. As shown in Figure 11, the flow expelled from each nozzle mixes in the lower region of the pre-chamber. As this flow moves upstream, the turbulent kinetic energy dissipates and weakens.

Figure 15(b) illustrates the distribution of turbulent kinetic energy in the x-x' cross-section for Case 3, which exhibits the highest turbulence kinetic energy (TKE) level at the spark plug gap. In a PCSI engine, the turbulence intensity at the spark plug gap significantly impacts ignition stability, flame propagation, and combustion efficiency by influencing flame kernel formation, cycle-to-cycle variations, and emissions. Hence, maintaining high TKE at the spark plug gap through pre-chamber geometry optimization is crucial, as it enhances flame kernel development by increasing the initial

 doi:10.20944/preprints202503.0200.v1

flame stretch rate and reducing ignition delay [14,18,19]. It can be observed that the formation of two recirculation zones on the left and right sides of the pre-chamber, where TKE levels are significantly low. A strong upwash flow with high turbulent kinetic energy develops between these two recirculation regions but weakens further as it moves toward the upper end of the pre-chamber. Eventually, this flow passes through the spark plug gap.

These findings indicate that to ensure an optimal distribution of turbulent energy at the spark plug gap for stable combustion, it is necessary to optimize the nozzle diameter and length, as well as the volume and shape of the pre-chamber.

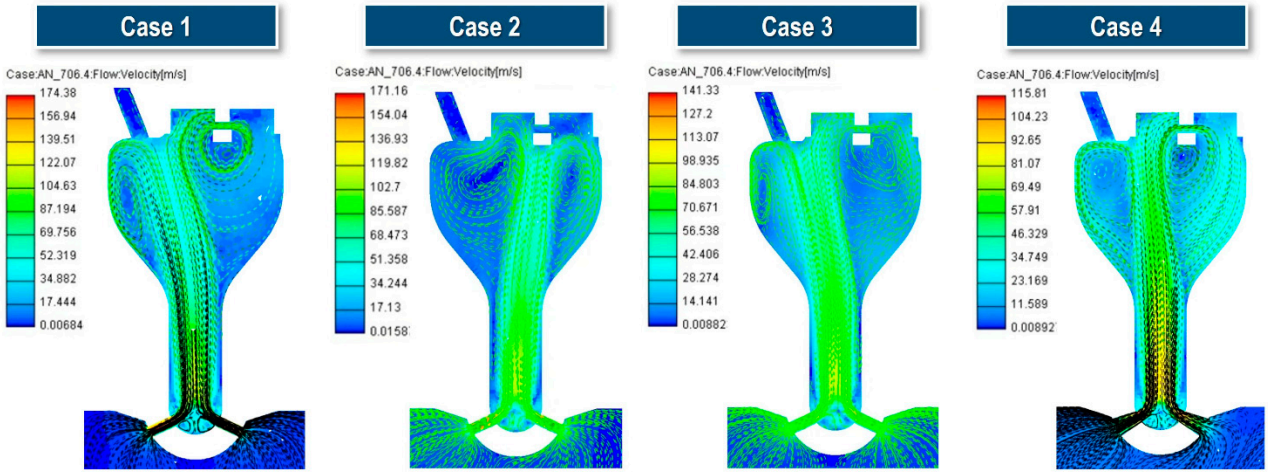

Figure 14. Flow distributions inside prechamber just before ignition for various cases(x-x' section).

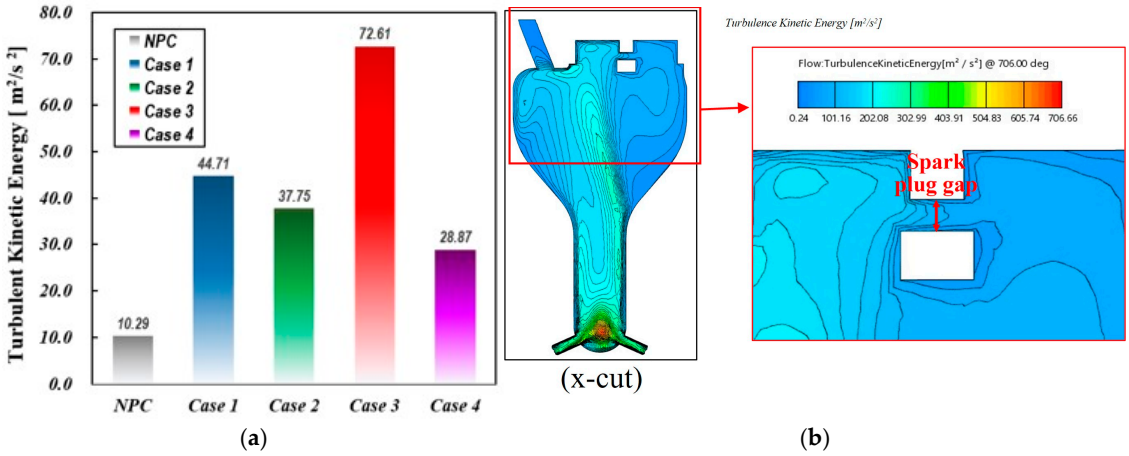

Figure 15. Comparison of averaged turbulent kinetic energy of the spark plug gap position before ignition (a) averaged turbulent kinetic energy of the spark plug gap position; (b) Sectional view of turbulent kinetic energy contour in prechamber for case 3.

Figure 16(a) presents the average jet penetration velocity, determined by measuring the distance traveled by the jet from the start of ejection until it either reaches the combustion chamber wall or ceases further movement. Among the analyzed cases, Case 3 exhibits the highest penetration velocity, attributed to its greater absolute mass flow and, consequently, stronger pre-chamber ejection momentum. Regarding nozzle diameter effects, it is well established that jets from smaller nozzle diameters penetrate the combustion chamber more rapidly due to their higher velocity and momentum. However, Case 3, despite having a larger orifice diameter, maintains a thicker jet core, which enhances momentum retention over a longer distance. Additionally, a thicker jet plume improves entropy transfer to the main chamber, facilitating deeper penetration before jet dissipation occurs.

 doi:10.20944/preprints202503.0200.v1

Figure 16(b) compares the instantaneous jet exit velocity at the nozzle with the instantaneous jet head velocity at FR2. The jet exit velocity is derived from simulations by averaging velocity magnitudes along the jet axis within the nozzle length. The figure indicates that at FR2, the jet head velocity decreases by approximately 2% to 26% relative to the jet exit velocity, reflecting the degree of deceleration. Among the examined cases, Case 4 demonstrates the highest jet speed ratio, signifying that the turbulent jet momentum is effectively sustained throughout the later stages of flame development. This is because the diverging-tapered-hole nozzle reduces pressure drop and boundary layer separation, thereby minimizing turbulence across the nozzle and producing stronger turbulent jets. This confirms that variations in jet head velocity are significantly influenced by pre-chamber nozzle geometry, as anticipated.

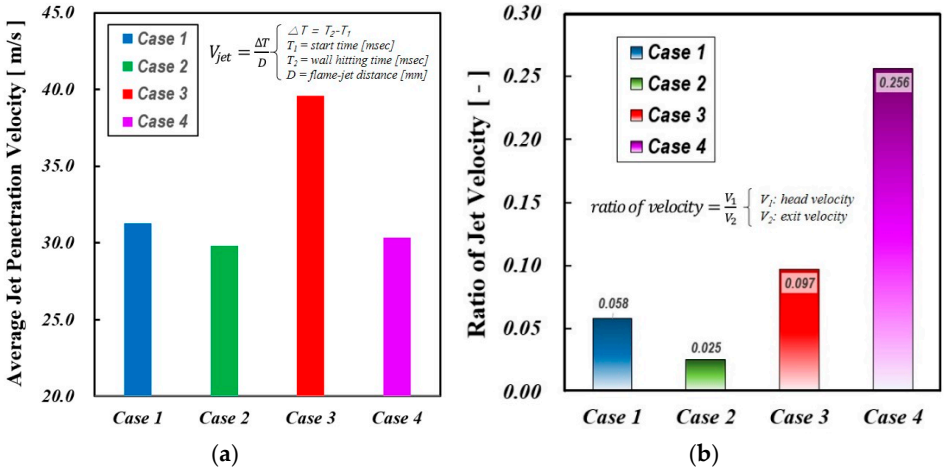

Figure 16. The effect of various geometric variation on jet velocity (a) average jet penetration velocity; (b) Ratio of jet velocity(@FR2).

Figure 17 presents a zoomed sectional view of the equivalence ratio distribution in the pre-chamber (PC) and main chamber (MC) just before ignition (706.4° CA) for various cases. During the compression stroke, as the piston moves upward and the pressure in the MC exceeds that of the PC, the lean mixture from the MC begins to penetrate into the PC. Upon entering through the orifices or nozzles, the lean mixture undergoes intense mixing in the lower region of the PC, forming a distinct upward-moving gas column. The velocity and trajectory of this gas column are strongly influenced by the orifice geometry.

As illustrated in Figure 17, this lean mixture column remains only partially mixed with the rich mixture in the PC until ignition occurs, which is a significant observation. Additionally, a non-uniform equivalence ratio distribution is evident around the spark plug region. These findings indicate that geometric parameters such as nozzle diameter and cone angle strongly affect both the trajectory and velocity of the lean mixture column from the MC, ultimately influencing the local fuel-air ratio at the spark plug gap.

These results suggest that modifications to the orifice geometry not only alter the fluid dynamic behavior of the turbulent jet but also influence the formation of pollutant emissions, such as CO and NOx. Furthermore, Figure 17 illustrates that the concentration of the mixture entering through each orifice varies among cases, and the resultant gas column's momentum and direction significantly affect the equivalence ratio distribution near the spark plug gap.

 doi:10.20944/preprints202503.0200.v1

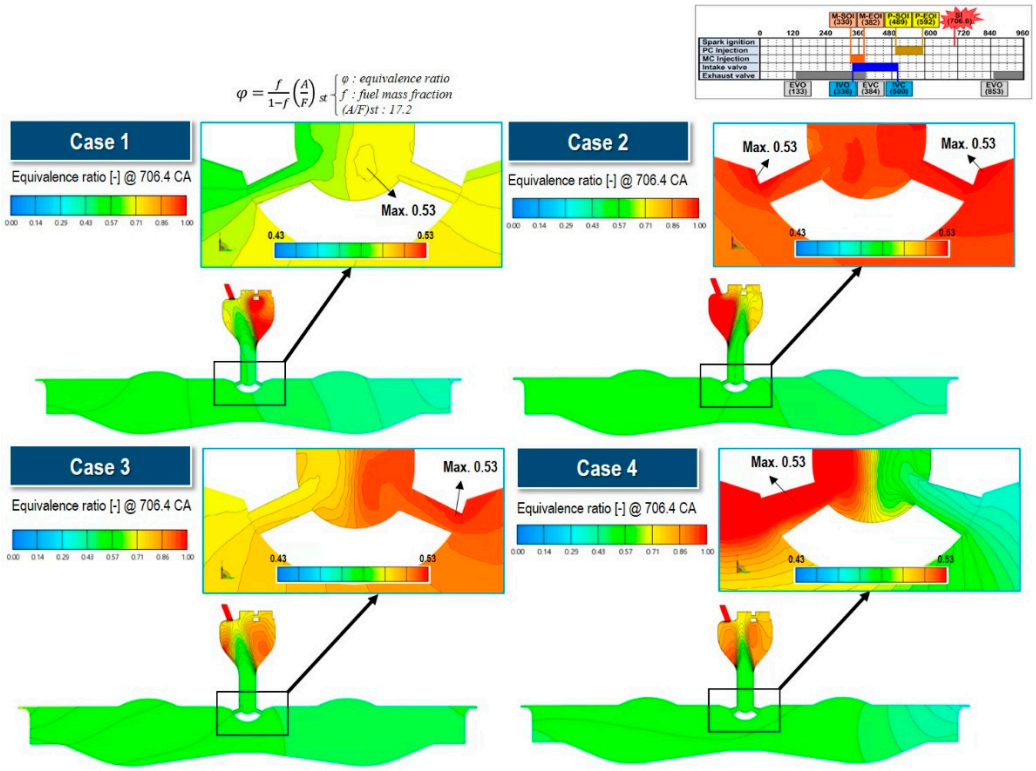

Figure 17. Equivalence distribution in pre and main chamber just before ignition for various cases (x-x' section).

In a PCSI engine, the residence time of gases in the pre-chamber significantly influences the mass of residual gases and the chemical composition of species such as CO, NO, OH radicals, and CO_2. Figure 18 presents (a) the amount of residual gas remaining in the pre-chamber (PC) from the previous cycle and (b) the chemical composition of the residual gas in percentage. As shown in Table 3, the amount of residual gas is not directly proportional to the residence time of the mixture in the PC. Case 1 exhibits the highest amount of residual gas, which is 10.8 times higher than that of Case 2. This is primarily due to the increased flow resistance caused by the reduction in orifice diameter. However, despite having the same orifice diameter as Case 1, Case 2 significantly improved flow resistance by increasing the orifice cone angle. The residual gas amount in Case 3 is 9.8% of that in Case 1, while Case 4 has 10.5% of the residual gas compared to Case 1.

Meanwhile, Figure 20(b) illustrates the variation in the chemical composition of residual gases due to changes in orifice geometry. For NO, Case 1 exhibits the highest concentration, which can be attributed to the longer residence time, as prolonged exposure to high temperatures enhances NO formation reactions.

In the case of CO, Case 4 shows the highest concentration. As indicated in Table 3, Case 4 has the shortest residence time, leading to an increase in incomplete combustion products like CO within the pre-chamber. Additionally, the OH radical concentration is on the order of 10^{-6}, making it barely visible in the graph. Among the residual gases, Case 4 exhibits the highest OH radical concentration at 9.475×10^{-6} (%). As an intermediate species in the combustion process, the OH radical concentration exhibits complex behavior depending on residence time and temperature. Therefore, in Case 4, which has the shortest residence time, the elevated OH radical concentration is likely attributed to its formation during the combustion reaction.

 doi:10.20944/preprints202503.0200.v1

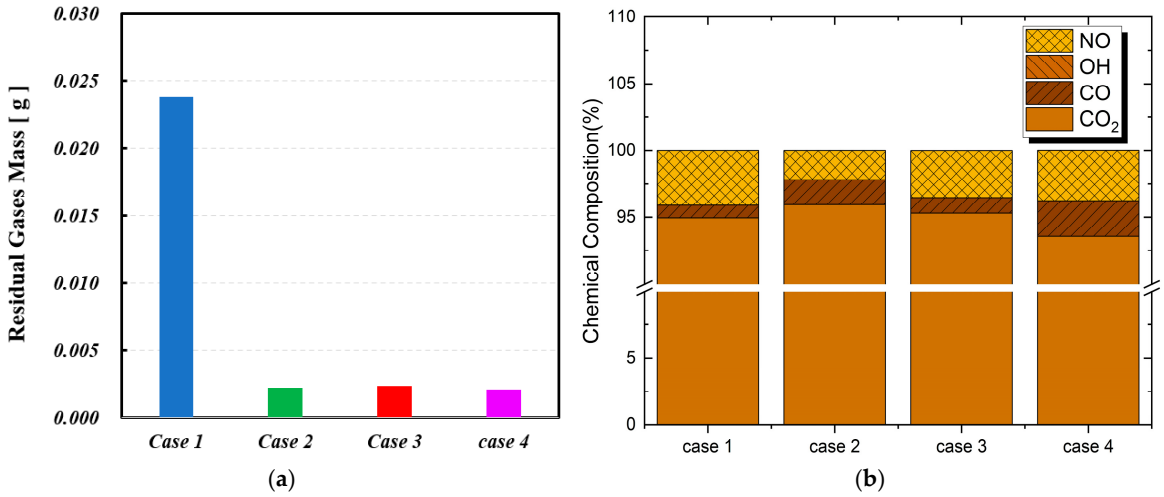

Figure 18. Mass(a) and chemical composition (b) of residual gas for different orifice geometries.

4.4. Effect of Geomatric Variations of Prechamber on Combustion Characteristics of Main Chamber

Figure 19 presents the cumulative heat release rate for various pre-chamber geometries, while Table 4 compares combustion durations across different cases. The inclusion of a non-pre-chamber (NPC) case highlights PCSI's impact on flame propagation and combustion timing. The results indicate that PCSI accelerates combustion initiation, with pre-chamber geometry significantly influencing early-stage combustion.

The CA0-10 duration (Phase 1), or flame development angle (FDA), represents the crank angle interval where 10% of the total fuel mass is burned. NPC exhibits the longest flame development duration (30.9 CA), nearly twice that of PCSI cases, indicating slower ignition, while Case 4 (12.7 CA) achieves the shortest Phase 1 duration, demonstrating the most efficient ignition, with Cases 1, 2, and 3 showing similar reductions (14.4–15.6 CA) compared to NPC.

During CA10-50 (Phase 2), pre-chamber jet influence weakens as combustion transitions toward a premixed flame regime, yet still affects overall flame propagation. The NPC case exhibits the fastest Phase 2 combustion (10.9 CA), while Case 4 has the longest duration (14.3 CA), indicating slower mid-stage combustion due to weaker jet penetration or a leaner main chamber mixture, whereas Cases 1, 2, and 3 show slightly shorter durations, suggesting improved combustion stability. The slower combustion rate in Phase 2 for Case 4 is primarily due to the weaker jet penetration, lower turbulence intensity, and leaner main chamber mixture, all resulting from the diverging-tapered-hole nozzle design. These factors collectively delay flame propagation and extend the mid-stage combustion duration.

NPC exhibits the longest Phase 3 duration (26.3 CA), indicating slow flame propagation due to possible flame quenching or incomplete oxidation. Among PCSI cases, Case 2 has the longest late-stage combustion (14.0 CA), while Cases 1 (13.4 CA) and 3 (13.3 CA) exhibit slightly faster combustion.

Case 3 exhibits the shortest total combustion duration (24.6 CA), indicating a well-balanced combustion process, while Case 4 has the longest (27.9 CA), suggesting a slower burn rate due to lower jet velocity and energy dissipation, which results in reduced turbulence and slower combustion progression. The NPC case (25.7 CA) shows a comparable CD to PCSI cases but demonstrates unstable combustion due to prolonged Phase 1 and Phase 3 durations. Overall, smaller orifice diameters enhance jet velocity, shortening early-phase combustion and improving pre-chamber charge ignition.

 doi:10.20944/preprints202503.0200.v1

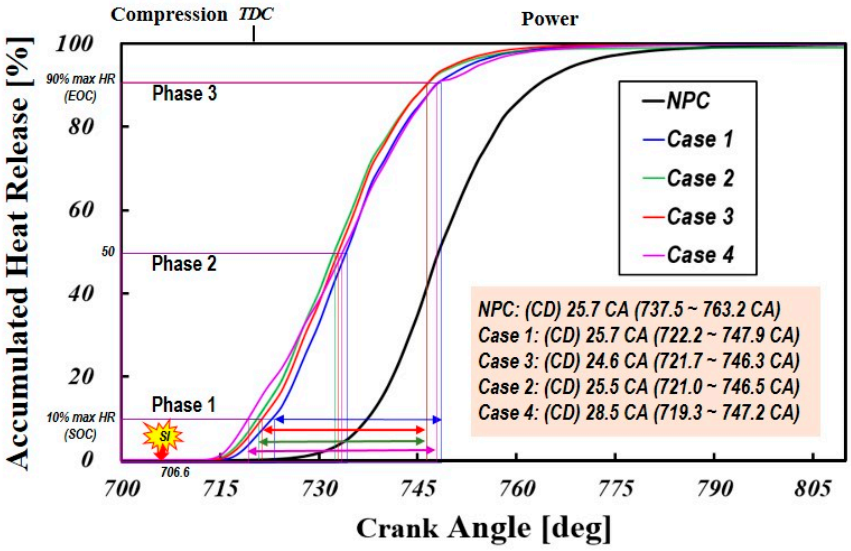

Figure 19. Profiles of accumulated heat release rate for various orifice geometries.

Table 4. Details of combustion durations for various cases (unit:CA).

case	Phase1 (0-10%)	Phase2 (10-50%)	Phase3(50-90%)	CD(10-90%)
Case 1	15.6[1]	12.3	13.4	25.7
Case 2	14.4	11.5	14.0	25.5
Case 3	15.1	11.3	13.3	24.6
Case 4	12.7	14.3	13.6	27.9
NPC	30.9	10.9	26.3	25.7

[1] unit is CA(Crank Angle).

Figure 20 presents the heat release rate (HRR) curves for four different orifice geometries throughout the combustion period, along with bottom-view flame surface density iso-contours at key combustion stages. Additionally, the figure includes pressure curves for both the PC and MC, as well as the pressure differential between the two chambers during the combustion process.

The HRR profiles in Figure 20(a-d) exhibit similar trends in terms of combustion initiation, duration, and completion, while also demonstrating a characteristic two-stage heat release process. The first peak occurs when PC jets merge and spread across the MC. Before merging, the PC jets reach their maximum flame surface area, contributing to the initial peak in the AHRR.

The second peak in AHRR is hypothesized to result from end-gas auto-ignition, which accelerates the consumption of the remaining unburned mixture. After the first peak, the PC jets merge into a hollow cone-shaped flame structure, leaving unburned air-fuel pockets between the hollow cone and the piston. Subsequently, compression due to ongoing heat release and upward piston motion triggers end-gas auto-ignition. Thus, the second peak in AHRR corresponds to this rapid auto-ignition event. These results are in exact agreement with experimental findings of previous literature from natural gas PCSI engines [54].

The first HRR peak is jet-momentum driven, suggesting a mixing-controlled premixed combustion phase. However, the scaling inconsistency of the second HRR peak and the absence of a significant driving pressure differential ($\Delta P \sim 0$) behind the pre-chamber jets suggest a transition from a mixing-controlled to a kinetically-controlled combustion regime. This transition coincides with the deceleration of pre-chamber jets due to diminishing driving pressure and charge entrainment, leading to a flame front evolution process wherein combustion is no longer solely mixing-driven. Unlike diesel combustion, where the rate-limiting factor is fuel-air mixing, pre-chamber combustion is governed by the interaction between hot burned gases and unburned fuel-air mixtures, rendering the process largely independent of laminar flame speed. The second-stage heat release is more intense and prolonged, primarily driven by bulk in-cylinder flow and turbulence, though as the main

 doi:10.20944/preprints202503.0200.v1

chamber mixture becomes leaner, combustion is increasingly influenced by chemical kinetics. In the later stages of heat release, combustion progression becomes less dependent on nozzle geometry, though nozzle-induced flow structures continue to play a role in determining flame propagation characteristics.

Previous studies indicate that main chamber ignition is inherently asymmetric, as combustion emerges from pre-chamber jets at different timings [41,54]. However, sequential flame surface density contour plots in Figure 20 reveal that flame propagation from each orifice remains largely uniform, likely due to the limited influence of large-scale turbulence in the main chamber. In contrast, during the early flame development stage, flame propagation exhibits non-uniform characteristics, as illustrated in Figure 22(a), where a long flame jet is observed near the spark plug in the initial moments of combustion onset.

As shown in Table 4, the flame development angles are 15.6 CA, 14.4 CA, 15.1 CA, and 12.7 CA in cases 1, 2, 3, and 4, respectively. Additionally, pre-chamber jet merging occurs most rapidly in Case 4, attributable to the diverging-tapered nozzle design, which accelerates jet dispersion and flame front interaction. Initial flame formation occurs between FR1 and FR2, where the flame divides into eight discrete jets upon exiting the pre-chamber nozzle holes and propagates individually. In Cases 1, 2, and 3, these eight jet flames merge gradually after FR2 (before TDC), whereas in Case 4, jet merging occurs significantly earlier due to the diverging-tapered-orifice design. In Case 4, the initial flame development phase is accelerated, leading to higher combustion rates before TDC (720° CA); however, after TDC, the heat release rate undergoes a sharp decline, causing a relatively delayed combustion progression.

Figure 20(b) illustrates that higher pre-chamber heat release and pressure buildup enhance jet penetration and kinetic energy dissipation, leading to the formation of turbulent mixing eddies in the main chamber. The impact of pre-chamber cone angle on jet dispersion is also evident, as a larger cone angle facilitates stronger jet interaction with the main chamber charge, further enhancing mixing efficiency. Notably, Case 3, as shown in Figure 20(c) which features an intermediate cross-sectional area of orifice, exhibits the most accelerated heat release in the early combustion stages, indicating an optimal balance between jet velocity and energy content. The orifice dimensions in Case 3 are sufficiently large to prevent jet flame quenching, ensuring stable combustion propagation.

A critical observation in Figure 20(d) is that the maximum jet driving force develops more rapidly in Case 4 than in other cases. This phenomenon arises due to the optimized spatial distribution of turbulent jets and shorter penetration depth, resulting in a larger flame jet angle, which promotes broader and shorter flame structures, increasing the probability of plume interaction. Additionally, the diverging-tapered nozzle increases the flow separation distance between the jet core and the nozzle wall, enhancing air entrainment into the nozzle and improving mixture formation within the main chamber. As a result, the radial velocity at the nozzle exits increases, contributing to improved mixture stratification. As combustion progresses, pre-chamber jet momentum decreases, transitioning from turbulent jet-driven propagation to a mushroom cloud formation mechanism. This transition results in faster jet head velocity decay, which slows the merged flame jet progression. Another distinct feature of Case 4 is the pronounced dip between the first and second heat release peaks, suggesting that pre-chamber jet combustion exhibits a weaker energy-carrying effect and a delayed ignition trigger compared to other orifice's geometries due to the fact that the expanding cross-section of the nozzle reduces jet penetration, leading to weaker turbulence and less effective charge mixing, delaying flame propagation. This disadvantageous combustion characteristic further exacerbates the retarded second-stage heat release, leading to extended total combustion duration relative to other nozzle configurations.

Preprints.org (www.preprints.org) | NOT PEER-REVIEWED | Posted: 4 March 2025 doi:10.20944/preprints202503.0200.v1

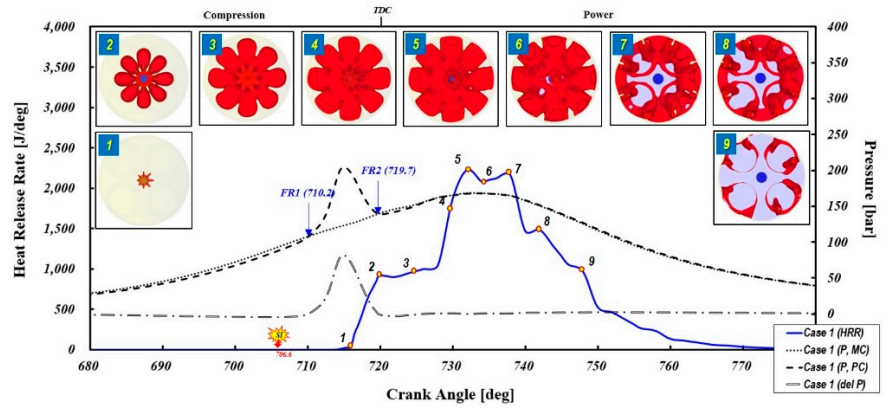

(**a**) case 1

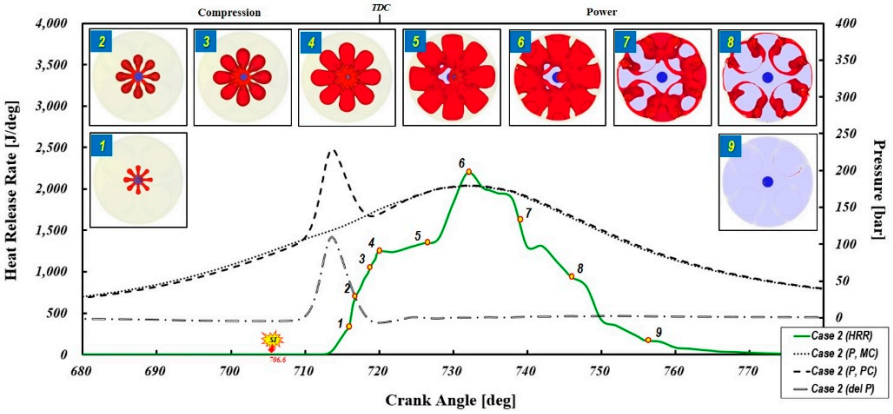

(**b**) case 2

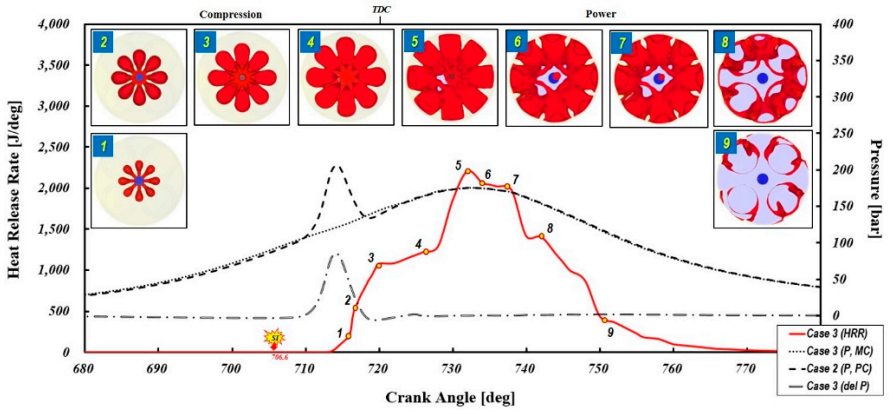

(**c**) case 3

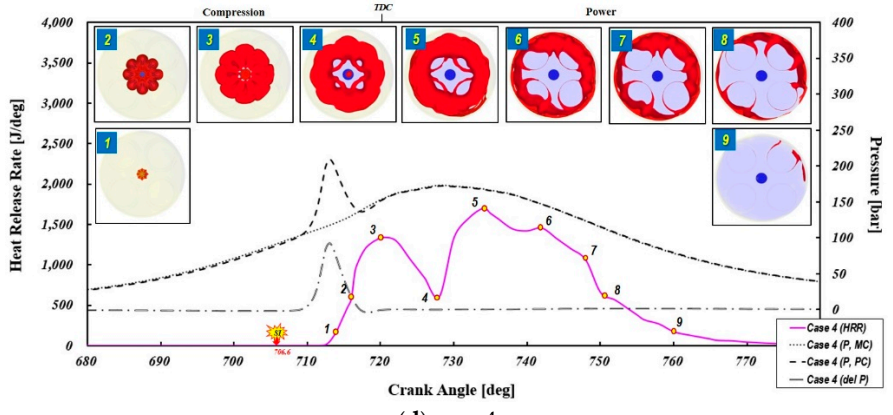

(**d**) case 4

Figure 20. Sequential plots of: heat release rate along with main-chamber pressure, pre-chamber pressure, pressure difference an d flame surface density contour from the bottom view (a) case 1; (b)case 2; (c)case 3; (d)case 4.

 doi:10.20944/preprints202503.0200.v1

4.5. Analysis of Chemical Composition and Emission Characteristics

Figure 21(a-d) presents the major chemical species formed in the pre-chamber across various cases, providing insight into the timing and characteristics of flow reversal from the main chamber to the pre-chamber. The plots illustrate the mass fraction relative to the instantaneous total mass, where each time step accounts for the dynamically updated total mass. These traces illustrate the temporal evolution of fuel and intermediate species critical to the ignition and combustion processes. Vertical dashed red lines indicate flow reversal events. The box in the upper right corner of each graph provides a magnified view of the residence time interval between the two backflow events. As previously established, the throat diameter is a critical parameter influencing pre-chamber peak pressure. A smaller orifice diameter increases residence time, allowing for a greater pressure buildup, whereas a larger orifice diameter facilitates earlier pressure relief, modifying combustion phasing. Combustion in the pre-chamber initiates as spark energy dissociates fuel and oxygen molecules, forming OH radicals. As shown in Figure 21(a-d), immediately after the start of spark, CH_4 rapidly depletes, causing OH radical formation. As combustion progresses, CO and OH concentrations peak at the first heat release peak (Figure 17), promoting CO oxidation to CO_2, which also reaches its maximum simultaneously. Since OH indicates reaction zones and heat release, it is a key parameter for analyzing flame structure and local fuel oxidation. The OH radical peak emerges within the residence zone, indicating the completion of pre-chamber charge combustion. If complete oxidation is not achieved, a significant portion of unburned hydrocarbons may be expelled during the exhaust stroke, adversely affecting combustion efficiency [19,29].

Following the second flow reversal (FR2), fresh charge and partially reacted species flow back into the pre-chamber, triggering localized combustion (post-flame reactions). This is confirmed by the second CH_4 peak after FR2, indicating that high pre-chamber temperatures facilitate secondary ignition and radical formation, leading to additional combustion events. Near FR2, CO oxidation halts before decreasing, attributed to declining OH radical concentration and temperature drop [12].

The temporal evolution and peak concentration profiles of OH radicals inside the pre-chamber exhibit no significant differences across the four orifice geometries. However, the maximum concentration and temporal evolution of CO show noticeable variations. This can be attributed to the fact that OH radicals are highly reactive intermediate species that rapidly reach a quasi-steady-state concentration during combustion. Additionally, since OH is continuously regenerated in reaction zones, its steady-state concentration remains relatively stable, independent of minor variations in orifice geometry.

In contrast, CO, as a combustion product, is strongly influenced by post-flame oxidation, residence time, and turbulence-driven mixing. Differences in orifice geometry affect flow dynamics, mixing intensity, and temperature distribution, leading to variations in CO oxidation rates.

In this study, Cases 1 and 2, which feature smaller orifices, increase flow restriction, prolong CO residence time, and result in higher CO accumulation. Conversely, Case 3, which has higher scavenging efficiency and greater turbulent mixing intensity, exhibits relatively lower CO emissions. However, OH radicals, being short-lived and equilibrium-driven, are less affected by these geometric variations, leading to minimal or no change in their concentration.

 doi:10.20944/preprints202503.0200.v1

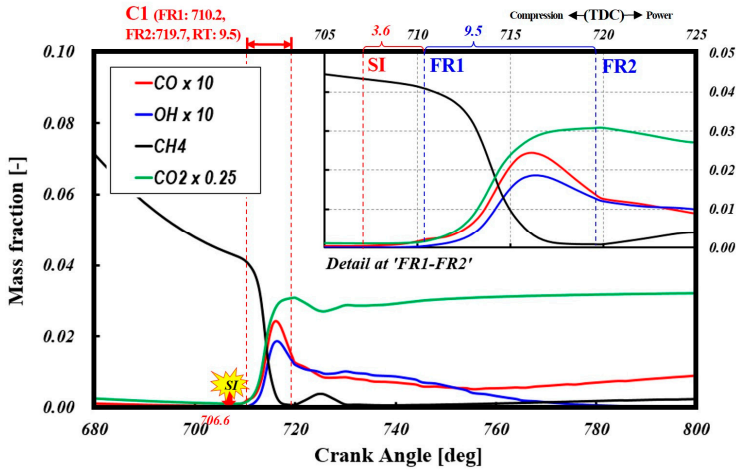

(a)

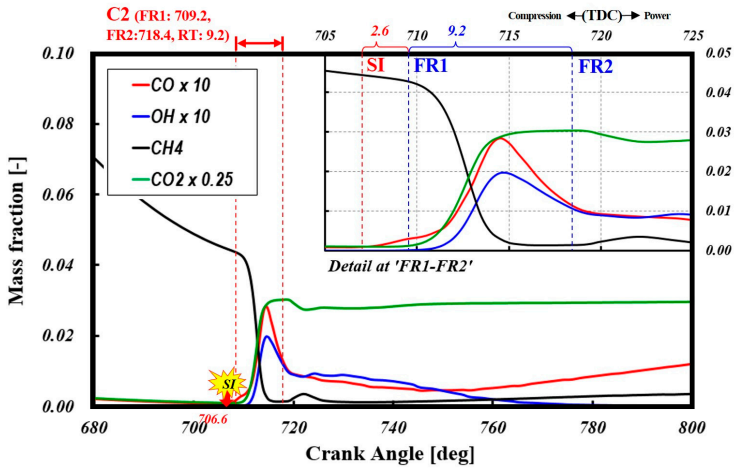

(b)

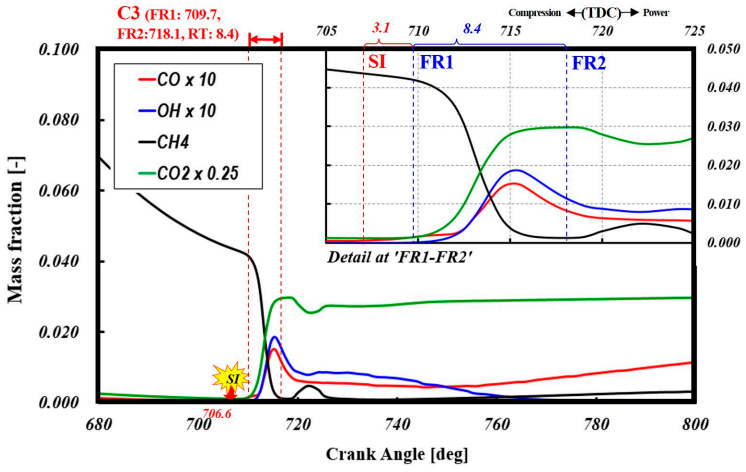

(c)

 doi:10.20944/preprints202503.0200.v1

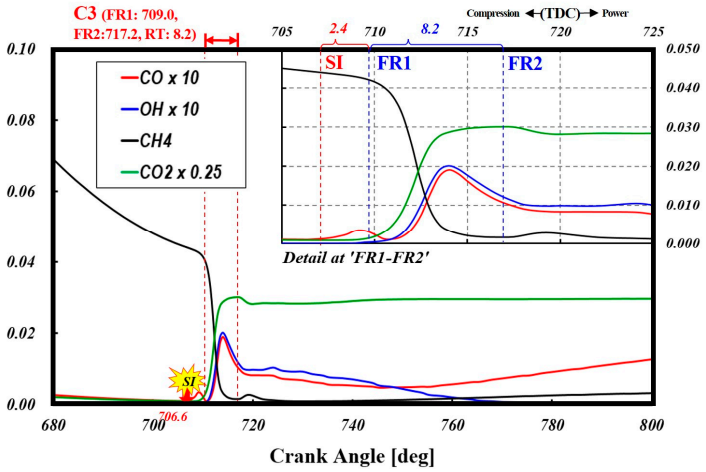

(**d**)

Figure 21. Temporal variations of the main chemical species mass fraction formed in the pre-chamber for various cases. (a) case 1; (b) case 2; (c)case 3; (d)case 4.

Figure 22 presents the flame development during the combustion period (712–732 CA) for four different orifice geometries in the y-y' cross-section, using iso-contours of flame surface density. A distinct feature observed is the occurrence of post-flame combustion after FR2, attributed to fuel and combustion product backflow from the main chamber into the pre-chamber. In Case 1, post-flame combustion initiates earliest (728 CA) compared to other cases due to the highest flow resistance from the main chamber to the pre-chamber, which delays the influx of fuel and combustion products. Specifically, a longer residence time interval delays the flow reversal (FR) event, resulting in later post-flame reactions. As shown in Table 3, Case 1, with the longest residence time, exhibits strong post-flame reactions downstream of the pre-chamber at 728 CA, whereas Case 4, with the shortest residence time, shows earlier post-flame reactions at 720 CA. Case 2 exhibits the fastest and most intense flame development, attributed to the highest PC-MC pressure difference, as observed in Figure 13. In Case 4, the diverging-tapered orifice produces the widest initial turbulent jet angle, leading to better spatial flame distribution during early flame development.

These findings indicate that lower resistance to reverse flow facilitates earlier post-flame combustion. Furthermore, post-flame ignition consistently occurs after FR2 due to fuel and combustion product entrainment into the pre-chamber.

 doi:10.20944/preprints202503.0200.v1

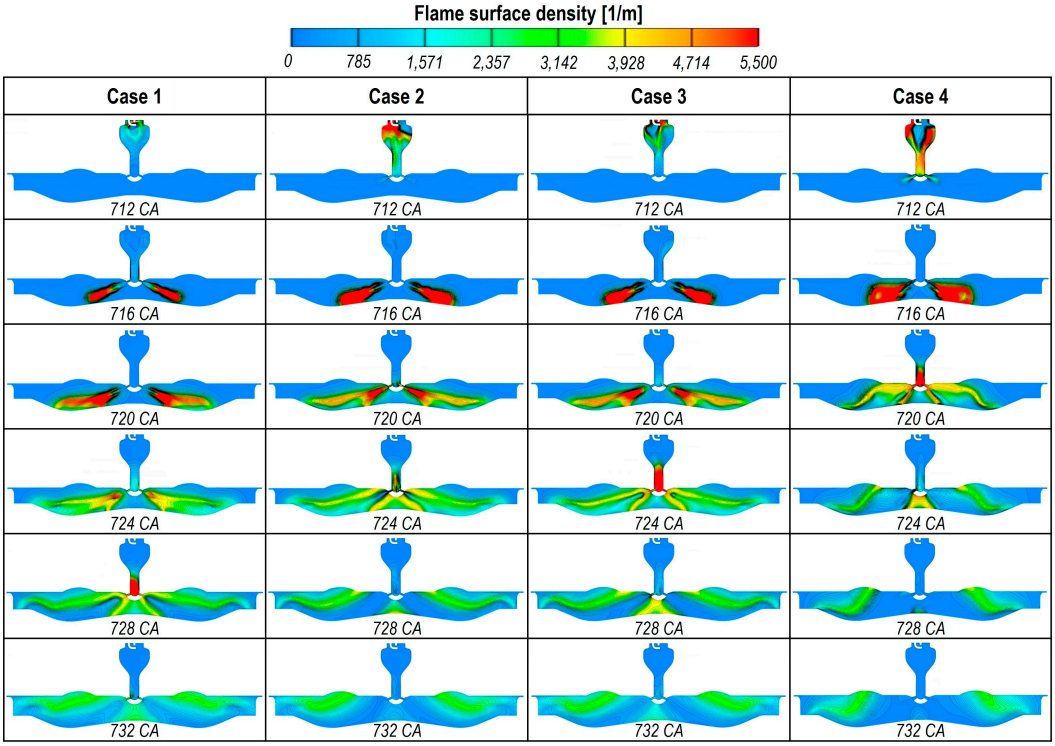

Figure 22. Temporal sequential plot of distribution of flame surface density in pre and main chamber.

Figure 23 illustrates the CH_4 consumption rate during residence time, along with the amounts of CO and NO produced during the gas residence time. As previously reported, a longer PC residence time tends to yield more complete combustion products than a shorter one, which directly influences the composition of the jets. The CH_4 consumption rate increases proportionally with residence time, and the amount of CO produced shows a similar proportional relationship. However, in case 3, improved turbulent mixing and the high turbulent kinetic energy near the spark plug gap—favorable for stable flame propagation, as shown in Figure 15(a)—result in a shorter residence time interval compared to case 2, yet the flames burn more completely. However, NO production does not exhibit the same proportionality with residence time. Because NOx emissions depend not only on residence time but also on factors such as the concentration distribution of the air-fuel mixture inside the pre-chamber, the presence of localized hot spots and rich pockets, and enhanced mixing that ensures complete combustion—thereby reducing UHC and CO while simultaneously suppressing NOx formation. Consequently, NOx generation in the pre-chamber is influenced by residence time as well as by factors such as higher turbulent kinetic energy, which accelerates chemical reactions by increasing mixing rates, and uniform mixing in the main chamber, which minimizes rich zones that contribute to NOx formation. As demonstrated in Figure 15(a) and Figure 17, case 3 exhibits the lowest NOx emissions by enhancing mixing through higher turbulent kinetic energy while avoiding the formation of excessive local rich pockets within the pre-chamber.

 doi:10.20944/preprints202503.0200.v1

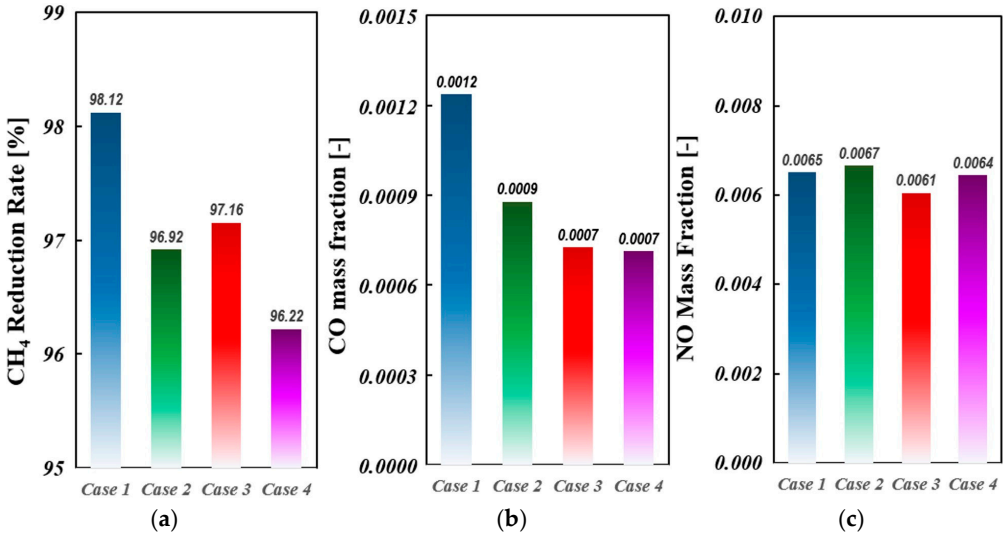

Figure 23. Variations of chemical compositions in prechamber during residence time. (a) consumption rate CH_4 (%); (b) production of CO during residence time; (c) production of NO during residence time.

The Figure 24 shows how NO forms and evolves over the combustion cycle within the PC and MC of a PCSI engine fueled by natural gas, comparing four different orifice (nozzle) geometries. Around the spark timing (near 706°CA), the flame initiates in the pre-chamber. As the flame expands, local temperature and pressure increase, promoting the formation of thermal NO. Any geometry that intensifies local heat release or creates high-temperature regions will tend to increase NO formation early in the combustion process. Noteworthy feature of Figure 24(a) is that that as the PCSI system approaches the FR2 timing, NO emissions gradually decrease. This occurs because a strong jet flow rapidly transfers combustion products into the main chamber, and the mixture is very lean, the peak NO level can be limited. Subsequently, when the main chamber pressure exceeds that of the pre-chamber, backflow occurs, allowing unburned fuel, active radicals, and combustion products to re-enter the pre-chamber. This backflow can initiate secondary ignition and radical formation, leading to additional combustion events and a sharp increase in NO emissions. After NO concentrations reach a peak, they then stabilize or "freeze," as combustion temperatures drop and mixing disperses the hot regions.

NO typically forms most rapidly at high temperatures and near-stoichiometric conditions. If the design prolongs high-temperature residence time in the pre-chamber (due to slower venting or less mixing), NO formation can continue to rise (case 1). The difference in final NO levels among the four cases reflects how effectively each orifice design manages local temperature, residence time, and mixing intensity. Figure 24(b) presents the temporal evolution profile of NO in the main chamber for case 2. In this case, the highest NO emissions are observed, which are attributed to the rapid temperature rise caused by strong auto-ignition and subsequent rapid combustion following the second peak of the heat release rate, as shown in Figure 20(b). In contrast, case 1 exhibits the lowest NO emissions; as indicated in Figure 20(a), turbulent jets with higher entropy discharged into the main chamber promotes mixing and heat release over a broader area, thereby suppressing localized rapid temperature increases and maintaining a lower NO level. Cases 3 and 4 demonstrate that an increased effective flow area leads to a more uniform combustion distribution and suppresses prolonged high-temperature zones, resulting in lower NO peaks. These findings underscore that improved mixing through turbulent jets—by preventing localized rich zones and distributing heat more evenly—is critical for reducing NO emissions. Hence, in PCSI engines, the pre-chamber is not merely an ignition source for the main chamber charge; it is designed to generate large-scale mixing eddies or plumes that facilitate the consumption of the main chamber charge, and when optimized, it serves as an effective means to suppress emissions such as NO and CO.

 doi:10.20944/preprints202503.0200.v1

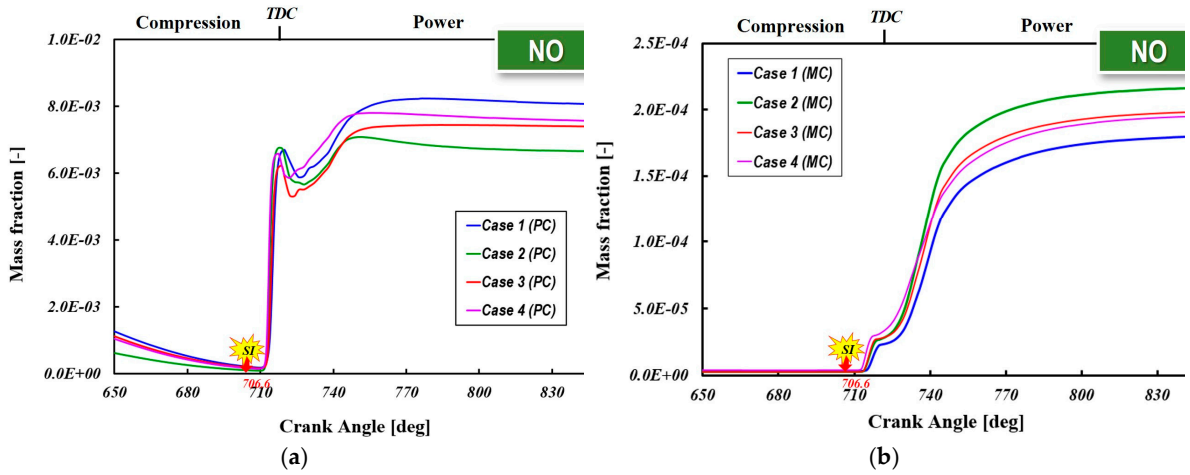

Figure 24. Temporal evolution of NO emission for four different orifice geometries. (a) pre-chamber; (b) main chamber.

Figure 25 displays bottom views of the in-cylinder mixture temperature distribution at 745°C for three cross-sectional areas indicated within the black box, for four different orifice geometries. Notably, localized hot spot zones exceeding 1800 K and quenching zones—resulting from turbulent jets impinging on the cylinder wall and piston surfaces—are clearly observed. These hot spot zones are generated by the interaction between the jets and the main chamber flow, and they may temporarily elevate temperatures, locally enhancing thermal NOx formation. Optimization of the orifice and pre-chamber volumes is required to mitigate localized NOx formation by distributing heat more evenly. In this study, the presence of eight orifices results in eight locally distributed quenching zones on the piston surface and the cylinder wall. The area and shape of each quenching zone differ because the momentum and flow rates of the hot jet plumes discharged from each of the eight orifices are not uniform, and these turbulent jets interact with the in-cylinder flow before reaching the quenching zones. The existence of these quenching zones, where combustion temperatures are relatively low, can lead to incomplete flame reactions, resulting in increased unburned hydrocarbon (UHC) and CO emissions. In contrast, in the case of Case 4, a quenching zone is not observed. This is attributed to the characteristics of the diverging-tapered orifice, as shown in Figure 20(d), where the flow velocity decreases slightly due to the expanding cross-sectional area, thereby reducing the penetration depth of the turbulent jet. Consequently, the combustion rate in the latter stages is significantly slower compared to other cases, which, due to the delayed reaction time, may increase the potential for NO formation. Ultimately, the CFD analysis in this study demonstrates that by coupling the simulation of the PCSI engine's emission characteristics with that of its in-cylinder thermal-fluid dynamics, the orifice and pre-chamber geometries can be optimized early in the design process, facilitating the development of high-efficiency, low-emission PCSI engines. However, to obtain more accurate results, there is a critical need to develop numerical models specifically tailored to lean conditions that account for turbulence–chemistry interactions and NOx emission mechanisms.

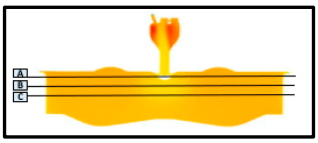

Section A Section B Section C

 doi:10.20944/preprints202503.0200.v1

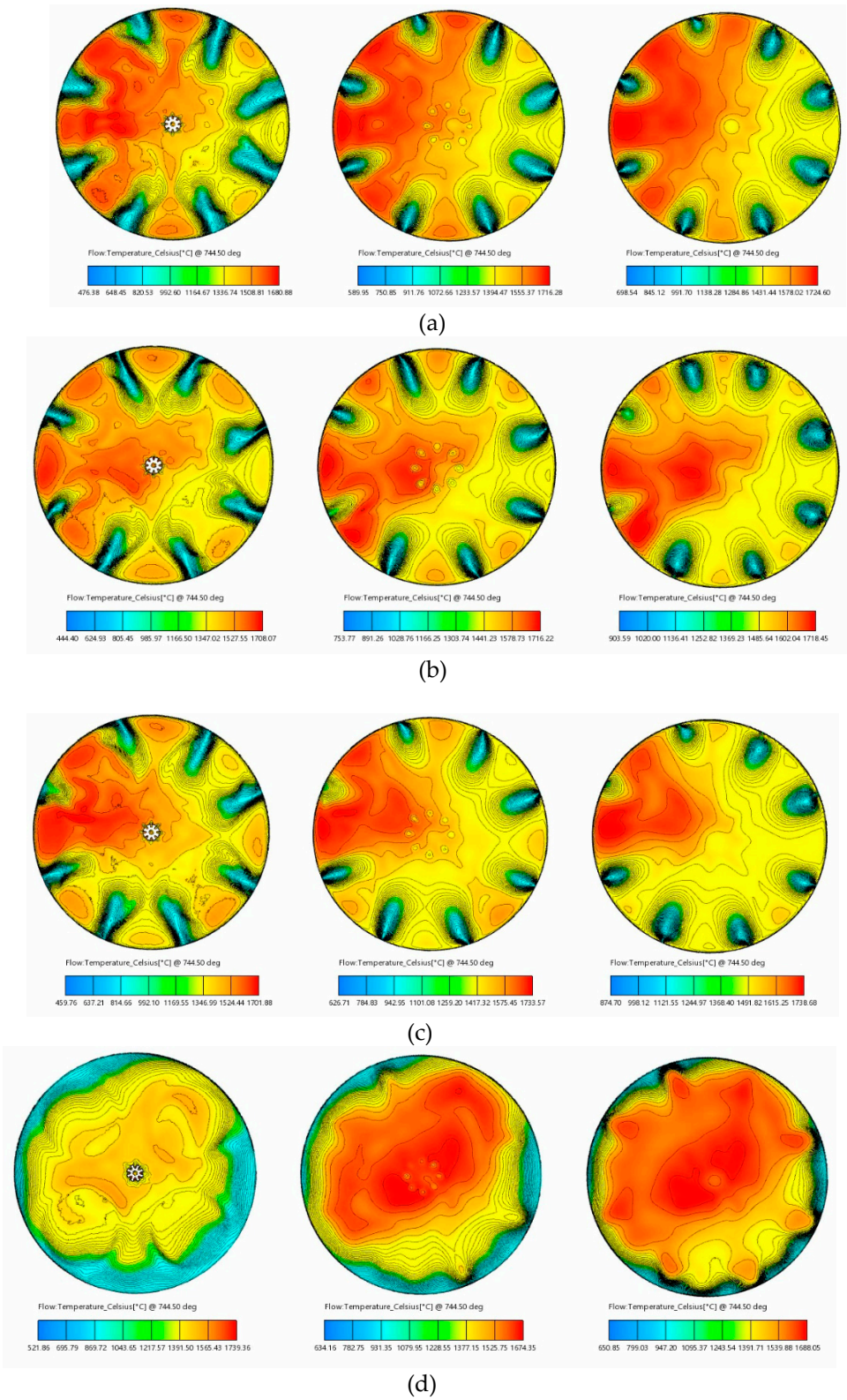

Figure 25. Multi-sectional plots of temperature distribution of in-cylinder mixture for four different orifice geometries: (a) case 1, (b) case2, (c) case3, (d) case 4 at 745deg.

5. Conclusions

In this study, a computational study combined with a set of measurements for experimental validation was performed to optimize the active pre-chamber geometry in a turbocharged eight-cylinder PFI SI engine. The main purpose of this paper is to improve knowledge of the active pre-chamber ignition system of full-scale real engine at real running condition. This study, therefore,

 doi:10.20944/preprints202503.0200.v1

focused on specifications such as pre-chamber volume, orifice diameter, orifice cone angle and diverging-tapered-nozzle, with a view to reducing emissions and improving combustion efficiency in large bore marine PCSI engine. Experimental validation confirms that optimized pre-chamber and orifice configurations reduce localized high-temperature zones, which in turn lowers NO emissions. By coupling detailed combustion simulations with experimental validation, this study underscores that enhanced turbulent mixing and proper management of dynamics are key to achieving lean-burn combustion with reduced pollutant formation. While further refinement of turbulence–chemistry interaction models is needed to improve NOx and CO predictions under ultra-lean conditions, the present work provides a robust framework for advancing PCSI engine design toward higher efficiency and lower environmental impact.

Author Contributions: For research articles with several authors, a short paragraph specifying their individual contributions must be provided. The following statements should be used "Conceptualization, S. J. J. ; methodology, S. J. J. ; software, S. J. J., S. J. M. ; validation, S. J. J. and S. P. S.; formal analysis, S. J. J.; investigation, S. J. J.; resources, S. J. J. and S. P. S.; data curation, S. J. J.; S. J. M. and S. P. S.; writing—original draft preparation, S. J. J.; writing—review and editing, S. J. J.; visualization, S. J. J. and S. J. M.; supervision, S. J. J.; project administration, S. J. J.; funding acquisition, S. J. J. All authors have read and agreed to the published version of the manuscript.

Funding: This work was supported by the Material and Parts Technology Development Project of the Korea Evaluation Institute of Industrial Technology, funded by the Korean government (Grant No. 20004900).

Data Availability Statement: Not applicable

Conflicts of Interest: The authors declare no conflict of interest.

References

1. Kirkpatrick, A.; Kim, G. H.; Olsen, D. CFD Modeling of the Performance of a Prechamber for Use in a Large Bore Natural Gas Engine. In *Proceedings of the ASME International Combustion Engine Division Spring Technical Conference*, Chicago, IL, USA, 11 November 2008; ICES2005-1049, pp. 397–403. https://doi.org/10.1115/ICES2005-1049
2. Payri, R., Novella, R., Barbery, I., & Bori-Fabra, O. Numerical and experimental evaluation of the passive pre-chamber concept for future CNG SI engines. Appl. Therm. Eng**.** **2023**, 230, 120754. https://doi.org/10.1016/j.applthermaleng.2023.120754
3. Riccardi, M., De Bellis, V., Sforza, L., Tunestål, P., Bozza, F., Beatrice, C., & Lucchini, T. (2023). Experimental and Numerical Analysis of an Active Pre-Chamber Engine Fuelled with Natural Gas. AE Technical Paper 2023-01-0185; SAE International: Warrendale, PA, USA, **2023**. https://doi.org/10.4271/2023-01-0185.
4. Winter, H., Schnessl, E., Pirker, G., Zelenka, J., & Wimmer, A. (2018). Application of CFD Simulation to Optimize Combustion in Prechamber Gas Engines with Port Injection. In Proceedings of the ECCM-ECFD, 7th European Conference on Computational Fluid Dynamics, Glasgow, United Kingdom, 11-15 June **2018**.
5. Bigalli, S., Catalani, I., Balduzzi, F., Matteazzi, N., Agostinelli, L., De Luca, M., & Ferrara, G. (2022). Numerical investigation on the performance of a 4-stroke engine with different passive pre-chamber geometries using a detailed chemistry solver. Energies, 15(14), 4968. https://doi.org/10.3390/en15144968
6. Xue, Y.; Wang, P.; Zhao, Q.; Ji, S.; Yong, C.; Yin, W. Effect of Spark Timing on the Pre-Chamber Jet Ignition in a Lean-Burn Natural Gas Engine. *Int. J. Engine Res.* **2023**, *24*(8), 3556–3573. https://doi.org/10.1177/14680874231162919
7. Li, F., Zhao, Z., Wang, B., & Wang, Z. (2019). Experimental study of pre-chamber jet ignition in a rapid compression machine and single-cylinder natural gas engine. International Journal of Engine Research, 22(4), 1342-1356. https://doi.org/10.1177/1468087419883783
8. Wang, T., Zhang, L., Li, L., Wu, J., & Wang, H. (2022). Numerical comparative study on the in-cylinder mixing performance of port fuel injection and direct injection gas-fueled engine. Energies, 15(14), 5223. https://doi.org/10.3390/en15145223
9. Novella, R., Gómez-Soriano, J., Martinez-Hernandiz, P. J., Libert, C., & Rampanarivo, F. (2021). Improving the performance of the passive pre-chamber ignition concept for spark-ignition engines fueled with natural gas. Fuel, 290, 119971. https://doi.org/10.1016/j.fuel.2020.119971

 doi:10.20944/preprints202503.0200.v1

10. Kim, J.; Scarcelli, R.; Som, S.; Shah, A.; Biruduganti, M.S.; Longman, D.E. Numerical Investigation of a Fueled Pre-Chamber Spark-Ignition Natural Gas Engine. *Int. J. Engine Res.* **2021**, *23*, 1475–1494. [https://doi.org/https://doi.org/10.1177/14680874211020180]
11. Shapiro, E.; Ahmed, I.; Tiney, N. Advanced ignition modelling for pre-chamber combustion in lean burn gas engines. In Proceedings of Ignition Systems for Gasoline Engines: Internationale Tagung Zündsysteme für Ottomotoren, Berlin, Germany, 6–7 December 2018; p. 104.
12. Distaso, E.; Amirante, R.; Cassone, E.; De Palma, P.; Sementa, P.; Tamburrano, P.; Vaglieco, B. Analysis of the Combustion Process in a Lean-Burning Turbulent Jet Ignition Engine Fueled with Methane. *Energy Convers. Manag.* **2020**, *223*, 113257–113247. [https://doi.org/https://doi.org/10.1016/j.enconman.2020.113257]
13. Ashish Shah, P. Tunestål, B. Johansson (2015). CFD Simulations of Pre-Chamber Jets' Mixing Characteristics in a Heavy Duty Natural Gas Engine; SAE Technical Paper 2015-01-1890; SAE International: Warrendale, PA, USA, 2015. [https://doi.org/https://doi.org/10.4271/2015-01-1890]
14. Jeong, S.-J. CFD Simulation of Pre-Chamber Spark-Ignition Engines—A Perspective Review. Energies **2024**, 17, 4696-4985.
15. Xu, L.; Li, G.; Yao, M.; Zheng, Z.; Wang, H. Numerical Investigation on the Jet Characteristics and Combustion Process of an Active Prechamber Combustion System Fueled with Natural Gas. Energies **2022**, 15, 5356-5372.
16. Bolla, M.; Shapiro, E.; Tiney, N.; Kyrtatos, P.; Kotzagianni, M.; Boulouchos, K. Numerical Simulations of Pre-Chamber Combustion in an Optically Accessible RCEM; SAE Technical Paper 2019-01-0224; SAE International: Warrendale, PA, USA, 2019. https://doi.org/10.4271/2019-01-0224.
17. Mastorakos, E.; Allison, P.; Giusti, A.; De Oliveira, P.; Benekos, S.; Wright, Y.; Frouzakis, C.; Boulouchos, K. Fundamental aspects of jet ignition for natural gas engines. SAE Int. J. Engines **2017**, 10, 2429–2438.
18. Baumgartner, L.S.; Wohlgemuth, S.; Zirngibl, S.; Wachtmeister, G. Investigation of a Methane Scavenged Prechamber for Increased Efficiency of a Lean-Burn Natural Gas Engine for Automotive Applications; SAE Technical Paper 2015-01-0866; SAE International: Warrendale, PA, USA, **2015**.
19. Wang, M., Leng, X., He, Z., Wei, S. et al., "A Numerical Study on the Effects of the Orifice Geometry between Pre- and Main Chamber for a Natural Gas Engine," SAE Technical Paper 2017-01-2195, 2017, doi:10.4271/2017-01-2195.
20. Lu, C.; Song, E.; Xu, C.; Ni, Z.; Yang, X.; Dong, Q. Analysis of Performance of Passive Pre-Chamber on a Lean-Burn Natural Gas Engine under Low Load. J. Mar. Sci. Eng. **2023**, 11, 596. https://doi.org/10.3390/jmse11030596
21. Krajnović, J.; Sjerić, M.; Tomić, R.; Kozarac, D. A Novel Concept of Active Pre-Chamber Engine with a Single Injector – The Passive Main Chamber Approach. Appl. Therm. Eng. **2024**, 250, 123509.
22. Lopez, J. J.; Novella, R.; Gomez-Soriano, J.; Martinez-Hernandiz, P. J.; Rampanarivo, F.; Libert, C.; Dabiri, M. Advantages of the Unscavenged Pre-Chamber Ignition System in Turbocharged Natural Gas Engines for Automotive Applications. *Energy* **2021**, *218*, 119466.
23. Shah, A.; Tunestal, P.; Johansson, B. Effect of Pre-Chamber Volume and Nozzle Diameter on Pre-Chamber Ignition in Heavy Duty Natural Gas Engines; SAE Technical Paper 2015-01-0867; SAE International: Warrendale, PA, USA, **2015**.
24. Biswas, S.; Tanvir, S.; Wang, H.; Qiao, L. On Ignition Mechanisms of Premixed CH_4/Air and H_2/Air Using a Hot Turbulent Jet Generated by Pre-Chamber Combustion. *Appl. Therm. Eng.* **2016**, *106*, 925–937.
25. Kyrtatos, P.; Bolla, M.; Benekos, S.; Bardis, K.; Xu, G.; Kotzagianni, M.; Wright, Y.M.; Giannakopoulos, G.; Frouzakis, C.E.; Boulouchos, K. Advanced Methods for Gas-Prechamber Combustion Research and Model Development. In Proceedings of the 16th Conference, The Working Process of the Internal Combustion Engine, Graz, Austria, 28–29 September **2017**; pp.167–183.
26. Kim, J.; Scarcelli, R.; Som, S.; Shah, A.; Biruduganti, M.S.; Longman, D.E. Assessment of turbulent combustion models for simulating prechamber ignition in a natural gas engine. *J. Eng. Gas Turbines Power* **2021**, *143*, 091004.
27. Kim, J.; Scarcelli, R.; Som, S.; Shah, A.; Biruduganti, M.S.; Longman, D.E. Evaluation of Combustion Models for CFD Simulation of Pre-Chamber Ignition in a Natural Gas Engine. In Proceedings of the 11th U.S. National Combustion Meeting, Pasadena, CA, USA, 24–27 March **2019**.

 doi:10.20944/preprints202503.0200.v1

28. Li, W.; Ma, J.; Zhu, T.; Wei, H.; Pan, J. Nozzle Design of Plug-and-Play Passive Pre-Chamber Ignition Systems for Natural Gas Engines. Appl. Sci. **2023**, 13, 9468. https://doi.org/10.3390/app13169468
29. Silva, M.; Sanal, S.; Hlaing, P.; Cenker, E.; Johansson, B.; Im, H.G. Effects of Geometry on Passive Pre-Chamber Combustion Characteristics; SAE Technical Paper 2020-01-0821; SAE International: Warrendale, PA, USA, **2020**.
30. Posch, S.; Winter, H.; Zelenka, J.; Pirker, G.; Wimmer, A. Development of a Tool for the Preliminary Design of Large Engine Prechambers Using Machine Learning Approaches. *Appl. Therm. Eng.* **2021**, *191*, 116774.
31. Rao, A.; Liu, Y.; M, F. Numerical Simulation of Nitric Oxide (NO) Emission for HCNG-Fueled SI Engine Using Zeldovich, Prompt (HCN), and Nitrous Oxide (N_2O) Mechanisms Along with Error Reduction Novel Sub-Models and Their Classification Through Machine Learning Algorithms. *Fuel* **2023**, *333*, 126320.
32. Riccardi, M., De Bellis, V., Sforza, L., Tunestal, P. et al., "Experimental and Numerical Analysis of an Active Pre-Chamber Engine Fuelled with Natural Gas," SAE Technical Paper 2023-01-0185, **2023**, doi:10.4271/2023-01-0185.
33. Sanal, S., Echeverri Marquez, M., Silva, M., Cenker, E. et al., "A Numerical Study on the Effect of a Pre-Chamber Initiated Turbulent Jet on Main Chamber Combustion," SAE Technical Paper 2022-01-0469, 2022, doi:10.4271/2022-01-0469.
34. AVL. *AVL FIRE, Software Documentation,* Version 2021 R2; AVL: Graz, Austria, **2021**.
35. Hanjalić, K.; Popovac, M.; Hadžiabdić, M. A robust near-wall elliptic-relaxation eddy-viscosity turbulence model for CFD. *Int. J. Heat Fluid Flow* **2004**, 25, pp.1047-1051.
36. Durbin, P. A. Near-wall turbulence closure modeling without "damping functions". *Theor. Comput. Fluid Dyn*. **1991**, 3, 1-13.
37. Nzebuka, G. G.; Waheed, M. A. Thermal evolution in the direct chill casting of an Al-4 pct Cu alloy using the low-Reynolds number turbulence model. *Int. J. Therm. Sci*. **2020**, 147, 106152.
38. Wu, X.; Durbin, P. A. Numerical simulation of heat transfer in a transitional boundary layer with passing wakes. J. Heat Transfer **1999**, 122, pp.248-257.
39. Fonseca, L.; Braga, R.; Morais, L. F.; Huebner, R.; Valle, R. M. Tuning the Parameters of the ECFM-3Z Combustion Model for CFD 3D Simulation of a Two-Valve Engine Fueled with Ethanol. *SAE Tech. Pap.* **2016**, *2016-36-0383*. SAE International: Warrendale, PA, USA.
40. Meneveau, C.; Sreenivasan, K.R. The Multifractal Nature of Turbulent Energy Dissipation. *J. Fluid Mech.* **1991**, *224*, 429–484.
41. Benajesa, J.; Novellaa, R.; Gomez-Sorianoa, J.; Barberya, I.; Libertb, C.; Rampanarivob, F.; Dabirib, M. Computational assessment towards understanding the energy conversion and combustion process of lean mixtures in passive pre-chamber ignited engines. *Appl. Therm. Eng.* **2020**, 178, 115501.
42. Metghalchi, M.; Keck, J.C. Burning velocities of mixtures of air with methanol, isooctane, and indolene at high pressure and temperature. *Combust. Flame* **1982**, 48, pp.191–210.
43. Meneveau, C.; Poinsot, T. Stretching and quenching of flamelets in Premixed turbulent combustion. *Combust. Flame* **1991**, *86*, 311–332.
44. Veynante, D.; Vervisch, L. Turbulent Combustion Modeling. *Prog. Energy Combust. Sci.* **2002**, *28*, 193–266.
45. Hautman D.J.; Dryer F.L.; Schug K.P. Glassman I. A Multiple-step overall kinetic mechanism for the oxidation of hydrocarbons, *Combust. Sci. Technol.* **1981**, 25, pp.219-235.
46. Jay S.; Béard P.; Pires da Cruz A. Modeling Coupled Processes of CO and Soot Formation and Oxidation for Conventional and HCCI Diesel Combustion, SAE Technical Paper 2007-01-0162, **2007**, https://doi.org/10.4271/2007-01-0162.
47. Heywood J.B. Internal Combustion Engines Fundamentals, 2nd ed. Mc Graw Hill Publication, **2018**; pp.154-196.
48. Benson, R.S.; Horlock, J.H.; Winterbone, D.E. The Thermodynamics and Gas Dynamics of Internal-Combustion Engines, Vol. I, II; Clarendon Press: Oxford, UK, 1982.
49. Van Gerpen, J. Documentation of the Benson Diesel Engine Simulation Program; Technical Report 88-C-025; U.S. Army Aviation and Technology Activity-AVSCOM: Cleveland, OH, USA, **1988**.
50. Chiodi, M. An Innovative 3D-CFD-approach towards virtual development of internal combustion engines. Ph.D. thesis, Universität Stuttgart, Vieweg+Teubner Research Verlag, June **2010**.

 doi:10.20944/preprints202503.0200.v1

51. Tromellini, R., KUMAR, M., Moeeni, S., Chiodi, M. et al., "3D-CFD Full Engine Simulation Application for Post-Oxidation Description," SAE Technical Paper 2021-24-0016, **2021**, https://doi.org/10.4271/2021-24-0016.
52. Wanker, R. Simulation Methods Covering Recent Technologies for GDI Engines. In Proceedings of the AVL International Simulation Conference, Graz, Austria, 22–24 October **2019**.
53. Onofrio, G.; Napolitano, P.; Tunestal, P.; Beatrice C. Combustion sensitivity to the hole size in an active prechamber ultra-lean heavy-duty natural gas engine. Energy **2021**, 235, 121298.
54. Rajasegar, R.; Niki, Y.; Garcia-Oliver, J.M.; Li, Z.; Musculus, M.P.B. Fundamental insights on ignition and combustion of natural gas in an active fueled prechamber spark-ignition system. *Combust. Flame* **2021**, *232*, 111561.